NAVAL POSTGRADUATE SCHOOL
Monterey, California

THESIS

TWO-COLOR PHOTODETECTOR USING AN ASYMMETRIC QUANTUM WELL STRUCTURE

by

Kevin R. Lantz

June 2002

Thesis Advisor:	Gamani Karunasiri
Second Reader:	James Luscombe

Approved for public release; distribution is unlimited

THIS PAGE INTENTIONALLY LEFT BLANK

1. AGENCY USE ONLY *(Leave blank)*	2. REPORT DATE June 2002	3. REPORT TYPE AND DATES COVERED Master's Thesis		
4. TITLE AND SUBTITLE: Title (Mix case letters) TWO-COLOR PHOTODETECTOR USING AN ASYMMETRIC QUANTUM WELL STRUCTURE			5. FUNDING NUMBERS	
6. AUTHOR(S) Kevin R. Lantz				
7. PERFORMING ORGANIZATION NAME(S) AND ADDRESS(ES) Naval Postgraduate School Monterey, CA 93943-5000			8. PERFORMING ORGANIZATION REPORT NUMBER	
9. SPONSORING /MONITORING AGENCY NAME(S) AND ADDRESS(ES) N/A			10. SPONSORING/MONITORING AGENCY REPORT NUMBER	
11. SUPPLEMENTARY NOTES The views expressed in this thesis are those of the author and do not reflect the official policy or position of the Department of Defense or the U.S. Government.				
12a. DISTRIBUTION / AVAILABILITY STATEMENT Approved for public release; distribution is unlimited			12b. DISTRIBUTION CODE	

13. ABSTRACT *(maximum 200 words)*

The past twenty years have seen an explosion in the realm of infrared detection technology fueled by improvements in III-V semiconductor technology and by new semiconductor growth methods. One of the fastest growing areas of this research involves the use of bandgap engineering in order to create artificial quantum wells for use in Quantum Well Infrared Photodetectors (QWIPs). QWIPs have an advantage over other infrared detectors such as Mercury Cadmium Telluride (MCT) because they have larger bandgaps and are therefore stronger and cheaper to manufacture. This thesis introduces one method of "multi-color" detection through the use of an asymmetric quantum well structure in which all energy transitions are possible. The QWIP structure in this thesis was designed to detect a laser wavelength of 1.06 µm and a wavelength in the 8-10 µm atmospheric window.

The relevance of a detector that is tuned to these wavelengths is that it can be used on military aircraft as a laser spot tracker and an infrared imager providing much greater accuracy and dependability than older systems.

14. SUBJECT TERMS Quantum well, QWIP, Two-color detection, Infrared imager, Laser Spot Tracker, Transfer matrix method, Airy functions			15. NUMBER OF PAGES 89
			16. PRICE CODE

17. SECURITY CLASSIFICATION OF REPORT Unclassified	18. SECURITY CLASSIFICATION OF THIS PAGE Unclassified	19. SECURITY CLASSIFICATION OF ABSTRACT Unclassified	20. LIMITATION OF ABSTRACT UL

THIS PAGE INTENTIONALLY LEFT BLANK

TWO-COLOR PHOTODETECTOR USING AN ASYMMETRIC QUANTUM WELL STRUCTURE

Kevin R. Lantz
Ensign, United States Navy
B.S., The Ohio State University, 2001

Submitted in partial fulfillment of the
requirements for the degree of

MASTER OF SCIENCE IN APPLIED PHYSICS

from the

**NAVAL POSTGRADUATE SCHOOL
June 2002**

Author: Kevin R. Lantz

Approved by: Gamani Karunasiri
Thesis Advisor

James Luscombe
Second Reader/Co-Advisor

William B. Maier II.
Chairman, Department of Physics

THIS PAGE INTENTIONALLY LEFT BLANK

ABSTRACT

The past twenty years have seen an explosion in the realm of infrared detection technology fueled by improvements in III-V semiconductor technology and by new semiconductor growth methods. One of the fastest growing areas of this research involves the use of bandgap engineering in order to create artificial quantum wells for use in Quantum Well Infrared Photodetectors (QWIPs). QWIPs have an advantage over other infrared detectors such as Mercury Cadmium Telluride (MCT) because they have larger bandgaps and are therefore stronger and cheaper to manufacture. This thesis introduces one method of "multi-color" detection through the use of an asymmetric quantum well structure in which all energy transitions are possible. The QWIP structure in this thesis was designed to detect a laser wavelength of 1.06 μm and a wavelength in the 8-10 μm atmospheric window.

The relevance of a detector that is tuned to these wavelengths is that it can be used on military aircraft as a laser spot tracker and an infrared imager providing much greater accuracy and dependability than older systems.

THIS PAGE INTENTIONALLY LEFT BLANK

TABLE OF CONTENTS

THIS PAGE INTENTIONALLY LEFT BLANK

LIST OF FIGURES

LIST OF TABLES

THIS PAGE INTENTIONALLY LEFT BLANK

LIST OF SYMBOLS

A	device area
A_n, B_n	wavefunction coefficients in the nth layer
Ai	Airy function of the first kind
Bi	Airy function of the second kind
c	speed of light
C_{AB}	bowing parameter
e	fundamental charge
$\mathbf{\hat{e}}$	electric polarization unit vector
E	energy
E_g	energy gap
F	external electric field
$g(\hbar\omega)$	Lorentzian function
$\hbar$	reduced Plank's constant
I	incident photon flux
$\mathbf{k}$	transverse wave vector
k_n	wave vector in the nth layer
L	well width
$\mathbf{M}$	composite transfer matrix
m_b^*	barrier effective mass
m_e	electron mass
$\mathbf{M}_{if}$	transition matrix element
m_{hh}^*	heavy-hole effective mass
$\mathbf{M}_n$	transfer matrix in the nth layer
m_n^*	effective mass in the nth layer
N_d	doping concentration
n_r	index of refraction

$\mathbf{p}$	momentum operator
T	temperature
$u(\mathbf{r})$	bandedge cell periodic function
$V(z)$	potential height
V_n	potential height in the nth layer
V_p	interaction potential
W	transition rate
x	molar percentage
z	growth direction
$\alpha(\hbar\omega)$	absorption coefficient
Γ	full width half maximum value of the excited state
ε_0	electric permittivity
λ	transition wavelength
$\rho(E_f)$	joint density of states
$\boldsymbol{\rho}(x,y)$	direction vector in the xy plane
ψ	envelope wavefunction
$\boldsymbol{\Psi}(\mathbf{r})$	complete wavefunction
ω	angular frequency

ACKNOWLEDGMENT

The author would like to thank Professor Gamani Karunasiri for the countless hours of lecture and discussion on solid state physics and for the infinite patience that he showed throughout the entire thesis process. Professor Karunasiri has been an excellent mentor and a good friend.

THIS PAGE INTENTIONALLY LEFT BLANK

I.   INTRODUCTION

A.   QUANTUM WELL INFRARED PHOTODETECTOR (QWIP)

The past twenty years have seen an explosion in the realm of infrared detection technology fueled by improvements in III-V compound semiconductor technology and by new semiconductor growth methods such as molecular beam epitaxy (MBE) and metal organic chemical vapor deposition (MOCVD). These technologies have made it possible to create artificially structured superlattices for use in novel device applications. The QWIPs operate by absorbing incoming photons and exciting carriers from the ground state to an excited state, which is known as intersubband transitions and is shown schematically in Figure 1.1. These excited carriers, or photoelectrons, can then be used to create a photocurrent through the application of an external bias.
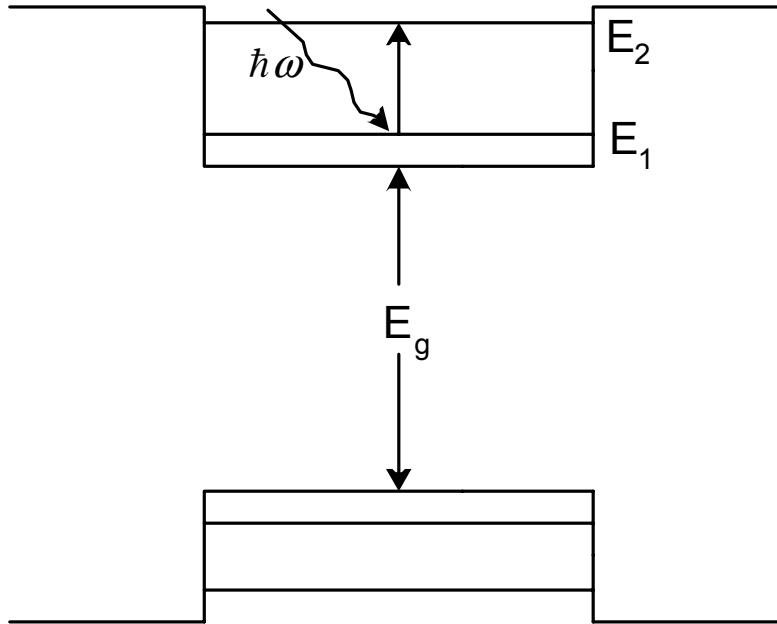
Figure 1.1   Diagram showing quantum well structure, energy levels (E_1, E_2), energy gap (E_g) and photon absorption $(\hbar\omega)$.

QWIPs have an advantage over other infrared detecting materials such as HgCdTe (MCT), which is shown in Figure 1.2, because they have much larger bandgaps and therefore are stronger and easier to manufacture. QWIPs also have an advantage

over MCT devices due to the fact that MCT devices utilize interband transitions, which limit the ability of the detector to be "tuned" to a specific wavelength. These advantages have made QWIPs the focus of recent infrared detection research.
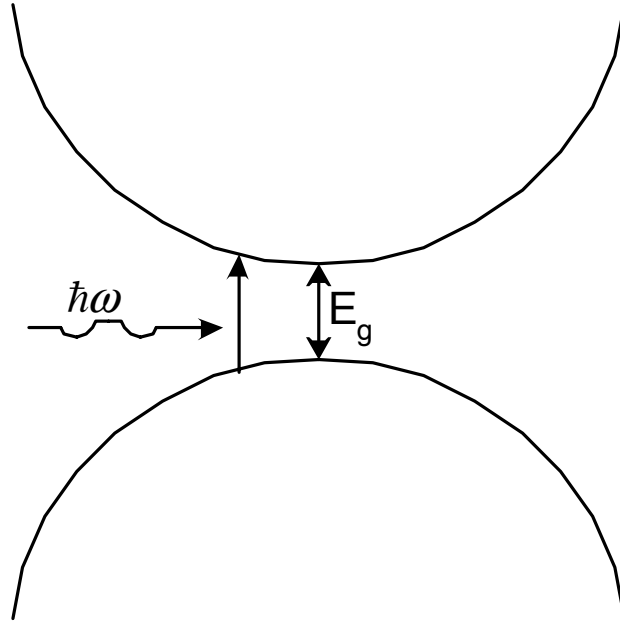
Figure 1.2   Diagram of HgCdTe bandstructure showing the energy gap and the photon absorption across the gap.

The idea of using semiconductors to create quantum wells was first proposed by Esaki and Tsu (1969) and since then many studies have been done on artificial quantum wells, which has led to a detailed understanding of energy-level spacing, intersubband and interband selection rules, line shapes and intersubband absorption. The earliest working QWIP was designed using GaAs/AlGaAs and was based on bound-to-bound transitions (Levine *et al.* 1987). The responsivity of this first device was extremely low because the photoelectrons had to tunnel through large barriers and therefore the device had to operate under a CO_2 laser. This low responsivity led to the use of bound-to-continuum transitions, which was first proposed by Coon *et al.* (1984). The first bound-to-continuum QWIP was demonstrated to have a much higher responsivity and a larger spectral width (Hasnain *et al.*, 1989), but had a small peak absorbance due to the continuum of states above the well.

Further advances in QWIP design have led to structures that are based on bound-to-quasi-continuum transitions (Levine *et al.*, 1991), bound-to-miniband transitions (Yu *et al.*, 1991) and bound-to-quasi-bound transitions (Gunapala *et al.*, 1996). These more recent configurations have shown good detector performance due to the fact that in all of these cases the ground state electrons do not flow in response to an external bias while the photoelectrons can create a photocurrent with the use of a relatively small bias. Multiple structural optimizations have also been made that improve QWIP performance. Increasing the barrier size has reduced the tunneling current by many orders of magnitude (Levine *et al.*, 1991), lowering the excited state from the continuum into the quasi-bound region has been shown to reduce the dark current from thermionic emission by a factor of ~12 at 70K (Gunapala *et al.*, 1996) and adding a grating on top of the device to increase the electric field polarization normal to the quantum wells in order to increase the absorption strength (Karunasiri *et al.*, 1995). All of these QWIPs have been shown to work well as infrared detectors, but they are limited to the detection of a narrow band of wavelengths. This limitation in QWIP technology has recently been overcome through the design of "multicolor", or multiple-wavelength, QWIPs.

Multicolor QWIPs are important because the peak wavelength emitted by an object shifts as its temperature changes. This shift in wavelength can cause performance limitations in single color QWIPs due to the peak radiation wavelength being far removed from the peak detection wavelength of the device, which will limit the discrimination ability of the detector. One way in which to improve this limitation is to design the QWIP to be sensitive to several wavelengths so that the emissivity changes of an object can be detected.

Some of the earliest methods of creating multicolor QWIPs were to build several stacks of square quantum wells, each with a different peak detection wavelength (Köck *et al.*, 1992, Gravé *et al.*, 1992, Liu *et al.*, 1993). The multicolor response of these stacks was achieved by attaching a contact to each stack (Köck *et al.*, 1992) or by controlling the external bias across the device to activate each stack sequentially (Gravé *et al.*, 1992, Liu *et al.*, 1993). Another method of creating a multicolor device was to use bandgap engineering technology to create an asymmetric quantum well, where the transitions from the ground state to several excited states are allowed and occur at differing wavelengths

(Berger *et al*., 1992, Martinet *et al*., 1992, and Chiang *et al*., 1996). The main advantage of using this system is that it requires only one set of quantum wells to achieve multicolor detection, but the downside is that in order to get the photoelectrons from the lower excited states out of the well a large bias has to be applied to the device, which increases the tunneling current. One method of overcoming this large tunneling current is to create a superlattice in which an asymmetric well is surrounded by multiple square wells so that the first miniband is aligned with the lowest excited energy level in the asymmetric well (Ting *et al.*, 1997). The advantage of this system is that photoelectrons in the lowest excited energy level have a higher mobility due to the presence of the miniband, and therefore the responsivity of this structure is greatly improved, but the complexity of the design makes fabrication more difficult.

B.   PURPOSE OF THIS THESIS

The purpose of this thesis is to design an asymmetric quantum well capable of detecting a laser wavelength of 1.06 μm and a middle infrared wavelength in the 8-10 μm range through the use of both intersubband and interband transitions. The scope of this research will cover several aspects of semiconductor technology including theoretical study of band structure, intersubband and interband transition selection rules, intersubband absorption, structural design of the quantum well, and modeling of the effects of an external bias on the quantum well.

The solution to the Schrödinger equation in a QWIP with finite potential heights cannot be solved analytically, but must be calculated using techniques such as the transfer matrix method (Vassel *et al.*, 1983, Lui *et al.*, 1986, Wang *et al.*, 1989). The transfer matrix method utilizes the continuity and boundary conditions of the wavefunctions to obtain the energy eigenvalues and wavefunctions numerically. These values are then used to determine the absorption spectrum of a device, which is useful in optimizing the device performance.

In order to achieve two-color detection, it is necessary to design a quantum well structure having two energy transitions corresponding to the two detection wavelengths. In a square quantum well, this is difficult because intersubband transitions can only occur

between states with opposite parity according to the selection rules. In addition, the transition probability drops rapidly as the quantum number of the excited state increases. Introducing an asymmetry into the quantum structure and thereby altering the parity of the wavefunctions and allowing all transitions to occur can overcome this restriction (Martinet *et al.*, 1992). The quantum well structure designed in this thesis makes use of both intersubband and interband transitions to achieve multicolor detection. This method differs from those studied in the past, which utilized only intersubband transitions to obtain multicolor detection (Köck *et al.*, 1992, Gravé *et al.*, 1992, Liu *et al.*, 1993, Ting et al. 1997). The advantages of the method used in this thesis are that the use of interband transitions allows for much shorter wavelength detection while the longer wavelengths can be detected using intersubband transitions. Furthermore, the asymmetry of the quantum well allows the excitation of electrons from the ground state to the first excited state in the conduction band. This allows for the extraction of the photoexcited electrons to occur at a lower bias, which reduces the dark current dramatically.

C. MILITARY RELEVANCE

A multicolor QWIP is relevant in the military today because it can be used as both an infrared imager and a laser spot tracker for use in laser-guided weapons delivery. The quantum well design utilized in this thesis is capable of detecting wavelengths as low as 1 μm and could easily be tuned for use with any combat laser designator wavelengths. In addition to the 1.06 μm laser wavelength, this quantum well is designed to simultaneously detect infrared radiation in the 8-10 μm range, supporting infrared imagery.

The applications of infrared and laser detection technology in the military are legion. Specific benefits of QWIP detector devices are immediately evident in the following case: Military airborne weapon systems often utilize a FLIR (Forward Looking InfraRed) for target acquisition and tracking and a laser target designator/range finder that are often co-located in a single weapons pod (e.g., LANTIRN) (Hewish *et al.*, 2002). Some aircraft, such as the F-18, also employ a laser spot tracker, which is located in a separate, externally mounted pod. The addition of the separate laser spot tracker

(LST) provides the pilot with a visual laser designation cue, which is especially useful when designation occurs from an offboard source (e.g., Special Ops, "Buddy lasing", etc.). The LST affords much greater accuracy and confidence in ordinance delivery while expanding employment options. However, boresight errors are inherent in a multi-pod system and degradations due to misalignment are common. Another disadvantage is the loss of an external weapons station for carriage of a sensor.

The quantum well detector design proposed in this thesis will provide an advantage to both airborne systems, which will lead to better accuracy and lethality. In a system such as LANTIRN, it will provide laser spot tracking capability where one currently does not exist. For aircraft such as the F-18, the introduction of a laser spot tracker into the weapons pod will not only eliminate boresight errors but also free up the weapons station often occupied by the laser spot tracker, resulting in lethality and survivability benefits.

II.   QUANTUM WELL STRUCTURE AND INTERSUBBAND ABSORPTION

A.   INTRODUCTION

Intersubband absorption is an important aspect in the design of an infrared detector and has been studied extensively using multi-band methods (Shik, 1992, Peng *et al.*, 1995, Flatté *et al.*, 1995) and also using band-mixing (Peng *et al.*, 1995). These methods for studying absorption are very sophisticated and may not be suitable for use in designing QWIPs. When quantum well structures are formed using large bandgap materials, the envelope function approximation can be used instead to provide a more simple approach to determining design parameters. In the envelope function approximation, the Schrödinger equation is solved by using the transfer matrix method, which has been discussed by several researchers (Vassel *et al.*, 1983, Lui *et al.*, 1986, Wang *et al.*, 1989) and has become the method most commonly used to model quantum well technology today. This chapter will cover the transfer matrix method, band structure, selection rules for energy transitions and intersubband absorption.

B.   TRANSFER MATRIX METHOD

The Schrödinger equation inside an infinite square potential well, which is shown in Figure 2.1, is given by:

$$-\frac{\hbar^2}{2m_e}\frac{\partial^2}{\partial z^2}\psi_n = E_n\psi_n \qquad (2.1)$$

where m_e is the mass of the electron, $\hbar$ is the reduced Planck's constant, z is the growth direction and ψ_n and E_n are the wavefunction and energy eigenvalues, respectively. Finding the solution to (2.1) is relatively easy due to the conditions that the wave functions must go to zero at the edges of the well and that the electron must be within the well. In this case the quantized energy levels have the values (West *et al.*, 1985):

$$E_n = \frac{\hbar^2 \pi^2 n^2}{2m_e L^2} \quad \text{for } n = 1,2,3...$$ (2.2)

where L is the width of the well. The wavefunctions in this case are given by

$$\psi_n(z) = \sqrt{\frac{2}{L}} \sin\left(\frac{\pi n z}{L}\right)$$ (2.3)

where the $\sqrt{\frac{2}{L}}$ term is known as the normalization factor and comes from the condition

that

$$\int_{-\infty}^{\infty} |\psi_n(z)|^2 \, dz = 1.$$ (2.4)
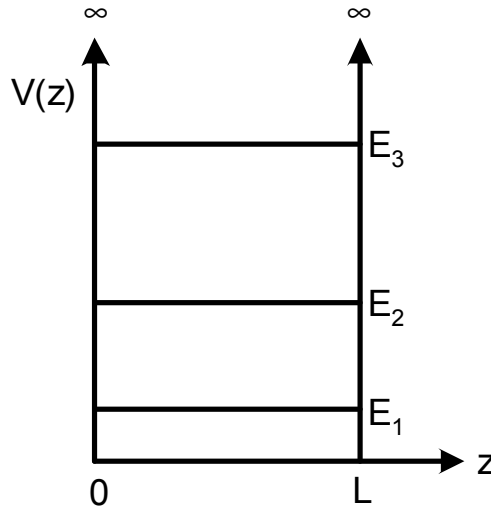
Figure 2.1   Schematic drawing of an infinite square quantum well with energy levels.

In the case of an infinite potential well the approach used above is relatively simple, but it becomes tedious and difficult to solve when multiple layers are added as in the case of a finite step quantum well (Yuh *et al.*, 1989). In this section the transfer matrix method will be discussed and shown to be able to handle potential wells with many layers.

In a heterostructure, the quantum well is formed by combining semiconductor materials that have differing bandgaps. The simplest form of this is a square quantum

well in which material A is surrounded by material B, which has a higher bandgap and which is thick enough not to allow for tunneling of the confined electron. In this case the electrons will be confined to the smaller bandgap region and using the envelope function approximation (also known as the effective mass approximation) the energy eigenvalues can be derived (Kane, 1957).

The envelope function approximation makes use of two assumptions; (1) that the potential difference between material A and B at the interface is localized (i.e. step function) and (2) the interface potential does not mix the band-edge wavefunctions, but shifts them. With these assumptions the wavefunctions take the form (Coon *et al.*, 1984)

$$\Psi(\mathbf{r}) = u(\mathbf{r}) e^{i\mathbf{k} \cdot \mathbf{\rho}(x,y)} \psi(z) \tag{2.5}$$

where $u(\mathbf{r})$ is the bandedge cell periodic function, z is the crystal growth direction, $e^{i\mathbf{k} \cdot \mathbf{\rho}(x,y)}$ is the plane-wave perpendicular to **z**, $\mathbf{\rho}(x,y)$ is the direction vector in the xy plane, **k** is the transverse wave vector, and $\psi(z)$ is the envelope wave function that satisfies the Schrödinger equation

$$\left(-\frac{\hbar^2}{2m^*(z)} \frac{\partial^2}{\partial z^2} + V(z) \right) \psi(z) = E\psi(z) \tag{2.6}$$

where $m^*(z)$ is the effective mass in the direction of growth and $V(z)$ is the potential height.

The transfer matrix method utilizes the piece-wise constant potential $V(z)$ to simplify much of the calculations of the envelope function approximation so that the wave functions in each layer are given as a linear combination of a right-traveling wave, $e^{ik_n z}$, and a left-traveling wave, $e^{-ik_n z}$, where k_n is the wave vector in the nth region (Note that k_n is real in the layer where $E_n > V(z)$ and imaginary otherwise). Using this fact and applying the boundary conditions

$$\psi_n(z_n) = \psi_{n+1}(z_n)$$

$$\frac{1}{m_n^*} \frac{\partial \psi_n(z_n)}{\partial z_n} = \frac{1}{m_{n+1}^*} \frac{\partial \psi_{n+1}(z_n)}{\partial z_n} \tag{2.7}$$

9

we can mathematically determine the energy eigenvalues.
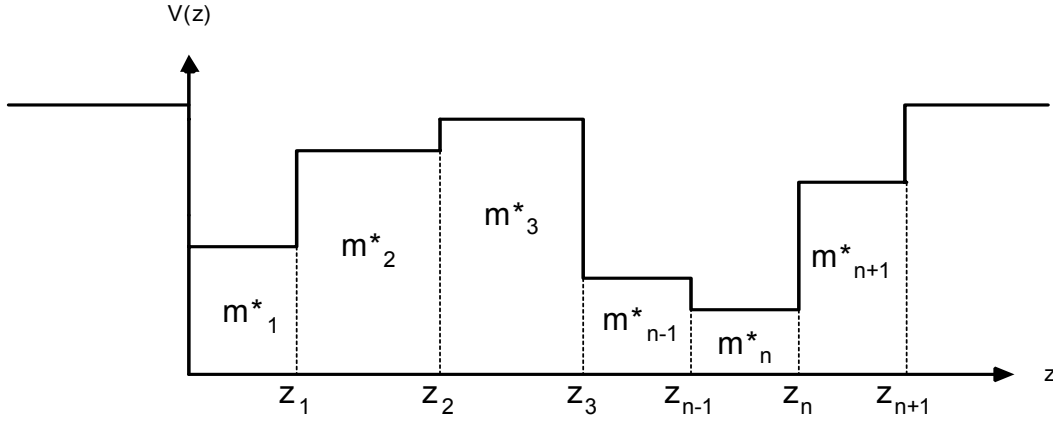
Figure 2.2   Arbitrary potential well of a multi-layered quantum well structure.

Figure 2.2 shows an arbitrary quantum well structure in which the thickness of each layer is given by $a_n = z_{n+1} - z_n$ and m_n^* is the effective mass of the electron in each region. The wavefunctions for each region are given by

$$\psi_n(z) = A_n e^{ik_n z} + B_n e^{-ik_n z} \qquad n = 0,1,2,...,n,n+1 \qquad (2.8)$$

where A_n and B_n are the coefficients of the left and right traveling wave in the nth region and the wave vector in the nth region is defined as

$$k_n = \sqrt{\frac{2m_n^*}{\hbar^2}(E - V_n)} \qquad (2.9)$$

where V_n is the potential height in the nth region. By applying the boundary conditions a relationship can be developed between the coefficients of the wavefunctions in neighboring regions.

$$\begin{bmatrix} A_{n+1} \\ B_{n+1} \end{bmatrix} = \mathbf{M}_n \begin{bmatrix} A_n \\ B_n \end{bmatrix} \qquad n = 1,2,...,N\text{-}1 \qquad (2.10)$$

where $\mathbf{M_n}$ is the transfer matrix for the interface at z_n

10

$$\mathbf{M}_n = \frac{1}{2} \begin{bmatrix} (1+\chi_n)e^{i(k_n-k_{n+1})z_n} & (1-\chi_n)e^{-i(k_n+k_{n+1})z_n} \\ (1-\chi_n)e^{i(k_n+k_{n+1})z_n} & (1+\chi_n)e^{-i(k_n-k_{n+1})z_n} \end{bmatrix} \qquad (2.11)$$

$$\chi_n = \frac{k_n m_{n+1}^*}{k_{n+1} m_n^*} \qquad (2.12)$$

From this formula a relationship can further be found between the first and the last region in the quantum structure

$$\begin{bmatrix} A_N \\ B_N \end{bmatrix} = \mathbf{M}_{N-1}...\mathbf{M}_2\mathbf{M}_1 \begin{bmatrix} A_1 \\ B_1 \end{bmatrix} = \mathbf{M} \begin{bmatrix} A_1 \\ B_1 \end{bmatrix} = \begin{bmatrix} m_{11} & m_{12} \\ m_{21} & m_{22} \end{bmatrix} \begin{bmatrix} A_1 \\ B_1 \end{bmatrix} \qquad (2.13)$$

where $\mathbf{M}$ is the composite transfer matrix for the entire structure and is given by

$$\mathbf{M} = \mathbf{M}_{N-1}...\mathbf{M}_2\mathbf{M}_1 = \begin{bmatrix} m_{11} & m_{12} \\ m_{21} & m_{22} \end{bmatrix}. \qquad (2.14)$$

If the potential heights in the two outer regions are higher than those in between them there will be bound energy states. For these bound states the wavefunctions must go to zero at $\pm\infty$ and this requirement means that $A_1 = 0$ and $B_N = 0$:

$$\begin{bmatrix} A_N \\ 0 \end{bmatrix} = \begin{bmatrix} m_{11} & m_{12} \\ m_{21} & m_{22} \end{bmatrix} \begin{bmatrix} 0 \\ B_1 \end{bmatrix}, \qquad (2.15)$$

which is satisfied when

$$m_{22}(E) = 0 \qquad (2.16)$$

Equation (2.16) is then tantamount to an eigenvalue condition on the allowed energies. We wrote a program to plot $m_{22}(E)$ versus E and locate the zeroes of the function, which determine the energy eigenvalues. The zeroes of $m_{22}(E)$ are found by searching for values of E such that $m_{22}(E)[m_{22}(E+\Delta E)] \leq 0$; in this way we know that the root lies between E and $E+\Delta E$. The accuracy of the eigenvalue is determined by ΔE; for most cases a value of $\Delta E = 1\ meV$ was used.

An example of the transfer matrix method for a square quantum well is shown in the next section, where the energy levels for the quantum well shown in Figure 2.3 are derived.
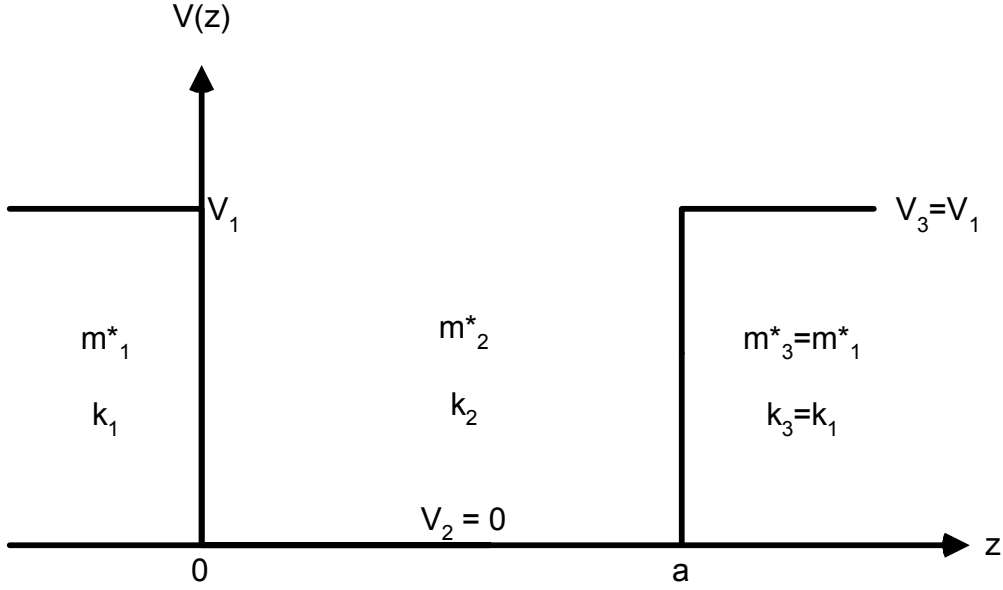
Figure 2.3   Schematic diagram of a finite square well with parameters used for calculation.

The composite transfer matrix **M** for this quantum well can be written as

$$\mathbf{M}=\mathbf{M}_2\mathbf{M}_1=\frac{1}{4}\begin{bmatrix}(1+\chi_2)e^{i(k_2-k_3)a} & (1+\chi_2)e^{-i(k_2+k_3)a} \\ (1+\chi_2)e^{i(k_2+k_3)a} & (1+\chi_2)e^{-i(k_2-k_3)a}\end{bmatrix}\begin{bmatrix}1+\chi_1 & 1-\chi_1 \\ 1-\chi_1 & 1+\chi_1\end{bmatrix} \quad (2.17)$$

where $k_3=k_1=i\kappa=i\sqrt{\dfrac{2m_1^*}{\hbar^2}(V_1-E)}$ and $k_2=\sqrt{\dfrac{2m_2^*}{\hbar^2}E}$, so that,

$$m_{22}(E)=\frac{1}{4}\left[(1-\chi_2)(1-\chi_1)e^{i(k_2+k_3)a}+(1+\chi_2)(1+\chi_1)e^{-i(k_2-k_3)a}\right] \quad (2.18)$$

The bound states occur when $m_{22}(E)=0$. Figure 2.4 shows a plot of $m_{22}(E)$ as a function of energy.
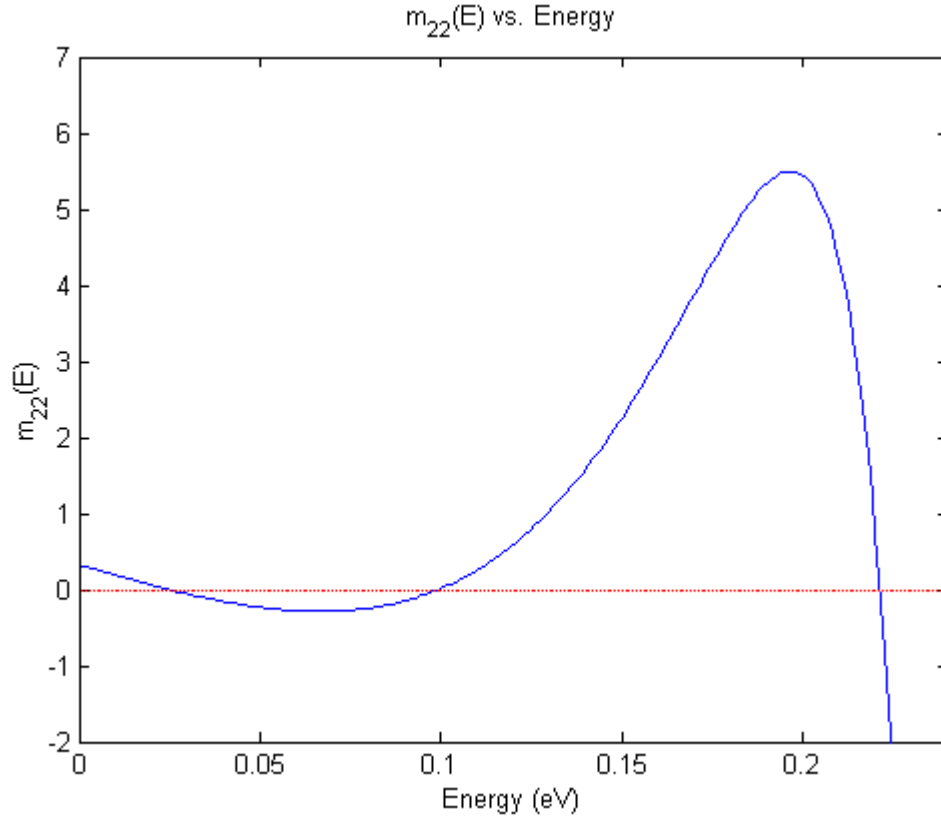
Figure 2.4   Plot of $m_{22}(E)$ versus E for $InP/In_{0.53}Ga_{0.47}As$ well with a = 150 Å.

Although only the conduction band was considered in this case, the valence band follows the same procedure and the energy eigenvalues in the valence band can be solved for with the same program keeping in mind that the effective masses and potential heights will differ in the valence band. Figure 2.5 shows the conduction band energy levels and wavefunctions of the quantum well in Figure 2.4.
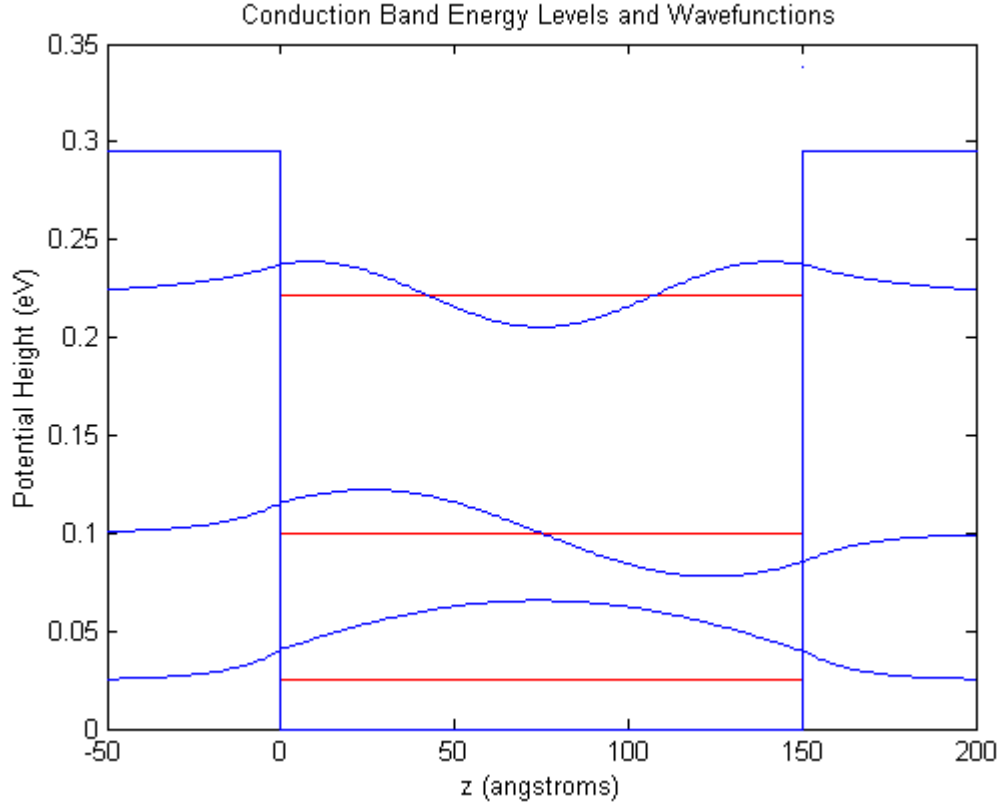
Figure 2.5   Conduction band energy levels and wavefunctions of the quantum well in
Figure 2.4.

C.   SELECTION RULES FOR OPTICAL TRANSITIONS

In a quantum well structure made of semiconductors, the wavefunctions consist of envelope and Bloch functions. This means that transitions between both Bloch and envelope states are allowed within the structure. Transitions between Bloch states correspond to interband transitions, while transitions between envelope states correspond to intersubband transitions. The transition rate for either interband or intersubband transitions is given as (Coon *et al.*, 1984)

$$W = \frac{2\pi}{\hbar} \sum_{i,f} |< \Psi_f \,|\, V_p \,|\, \Psi_i >|^2 \; \delta\left(E_f - E_i - \hbar\omega\right), \tag{2.19}$$

where E_i and E_f are the initial and final energy states and $\hbar\omega$ is the incoming photon energy. The initial and final wavefunctions in the transition rate are of the form of Equation (2.5),

14

$$\Psi_i = u_i(\mathbf{r})e^{i\mathbf{k}\cdot\boldsymbol{\rho}(x,y)}\psi_i(z)$$
$$\Psi_f = u_f(\mathbf{r})e^{i\mathbf{k}\cdot\boldsymbol{\rho}(x,y)}\psi_f(z)$$

$$(2.20)$$

The interaction potential V_p is defined in the dipole approximation as (Coon *et al.*, 1984)

$$V_p = \frac{e}{m^*}\left(\frac{I\hbar}{2\varepsilon_0 n_r \omega c}\right)^{1/2}\hat{\mathbf{e}}\cdot\mathbf{p}$$

$$(2.21)$$

where I is the incident photon flux, c is the speed of light, e is the electron charge, ε_0 is the electric permittivity, n_r is the index of refraction, ω is the angular frequency of the incoming photon, $\hat{\mathbf{e}}$ is the unit vector of the electric polarization of the incident light and $\mathbf{p}$ is the momentum operator. The integral in the transition rate is known as the transition matrix element, which is defined as

$$\mathbf{M}_{if} = \;<\Psi_f \,|\, V_p \,|\, \Psi_i> \;= \;<u_f(\mathbf{r})\psi_f(z)e^{i\mathbf{k}_f\cdot\boldsymbol{\rho}(x,y)}\,|\,V_p\,|\,u_i(\mathbf{r})\psi_i(z)e^{i\mathbf{k}_i\cdot\boldsymbol{\rho}(x,y)}>$$

$$= \;<u_f(\mathbf{r})e^{i\mathbf{k}_f\cdot\boldsymbol{\rho}(x,y)}\,|\,V_p\,|\,u_i(\mathbf{r})e^{i\mathbf{k}_i\cdot\boldsymbol{\rho}(x,y)}> \;<\psi_f(z)\,|\,\psi_i(z)>$$

$$(2.22)$$

$$+\;<\psi_f(z)e^{i\mathbf{k}_f\cdot\boldsymbol{\rho}(x,y)}\,|\,V_p\,|\,\psi_i(z)e^{i\mathbf{k}_i\cdot\boldsymbol{\rho}(x,y)}> \;<u_f(\mathbf{r})\,|\,u_i(\mathbf{r})>.$$

For the case of interband transitions ($\psi_i = \psi_v$, $\psi_f = \psi_c$) the second term in the transition matrix element is zero due to the orthogonality of the Bloch functions in the conduction and valence bands. On the other hand, the first term is zero for intersubband transitions ($\psi_i = \psi_1$, $\psi_f = \psi_2$) due to the fact that the Hamiltonian used to obtain ψ_f and ψ_i is Hermitian. Taking this into account, the transition matrix elements for both transitions are as follows

$$\mathbf{M}_{vc} = \;<u_c(\mathbf{r})\,|\,V_p\,|\,u_i(\mathbf{r})> \;<\psi_c(z)\,|\,\psi_v(z)>$$

$$(2.23)$$

$$\mathbf{M}_{12} = \;<\psi_2(z)\,|\,V_p\,|\,\psi_1(z)> \;<u_2(\mathbf{r})\,|\,u_1(\mathbf{r})>$$

where the $e^{i\mathbf{k}\cdot\boldsymbol{\rho}(x,y)}$ term, giving a delta function for the conservation of the xy plane momentum, has been dropped. It is easy to see that the only way to obtain non-zero

transition matrix elements is for both $<\psi_c(z)|\psi_v(z)>\neq 0$ and $<\psi_1(z)|V_p|\psi_2(z)>\neq 0$.
For a square quantum well this implies that only even-to-even or odd-to-odd interband transitions are possible, while for intersubband transitions, $V_p \propto \partial/\partial z$ and only even-to-odd or odd-to-even transitions are possible as shown in figure 2.6.
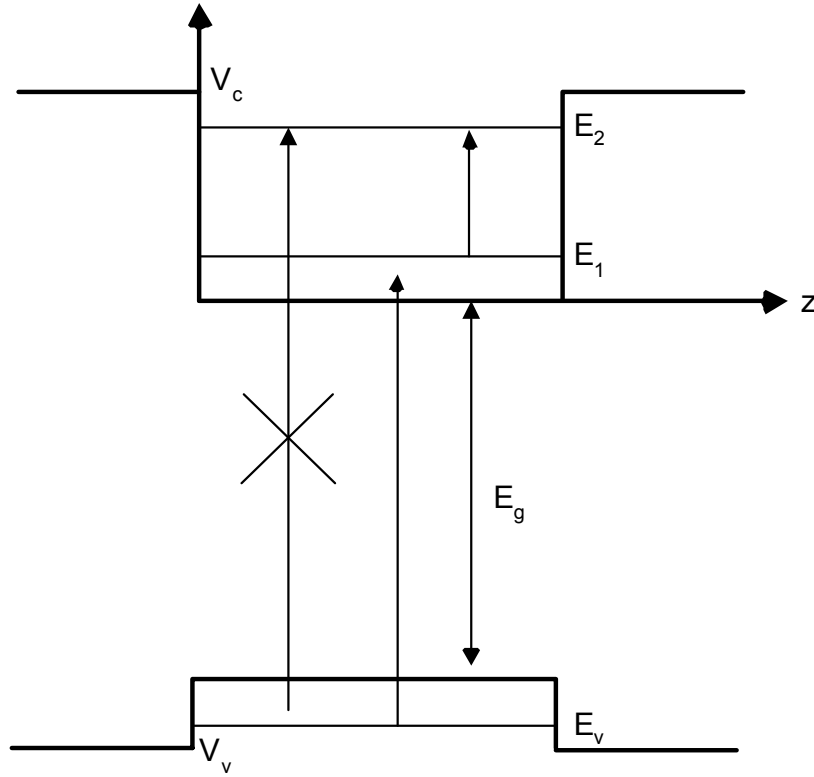
Figure 2.6   Schematic diagram of a square quantum well showing allowed and
forbidden (X) transitions.

If a step is added within the well in Figure 2.6 then the wavefunctions are no longer only even or odd, but a combination of the two. In this case the transition matrix elements will be non-zero for all transitions as is shown in figure 2.7.
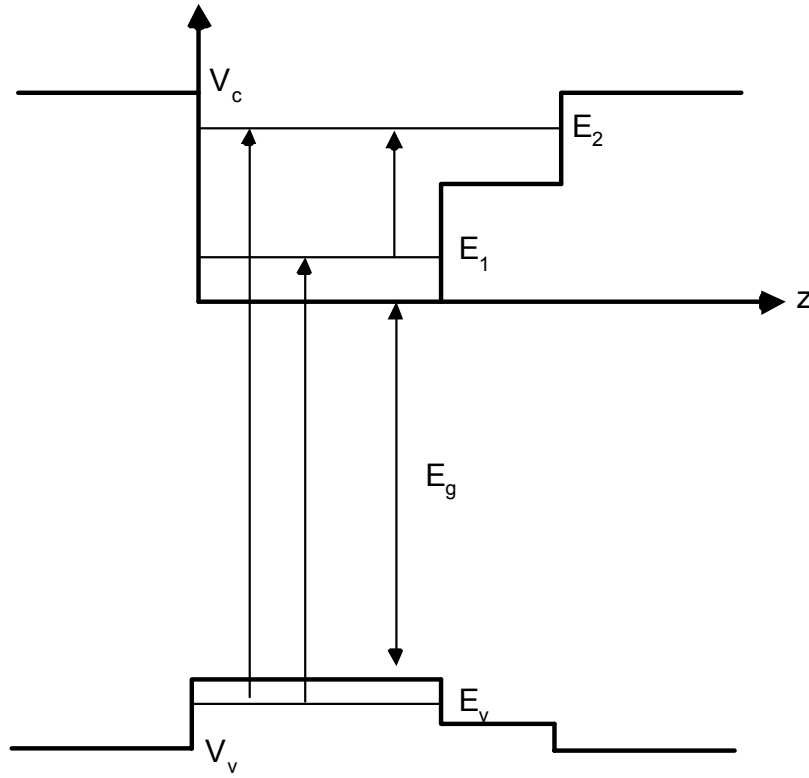
Figure 2.7   Schematic diagram of a step quantum well showing that all transitions are allowed.

This step is vital to this thesis because it allows for the excitation of electrons from the E_v and E_1 states to the E_2 state to be collected as photocurrent. The optimization of transition wavelengths and the transition probability are discussed in the next section.

D.   INTERSUBBAND ABSORPTION

Absorption is an important factor in the design of a multicolor infrared detector because it is one of the only measurable quantities of a sample. The absorption coefficient is proportional to the amount of incident light that is absorbed in the sample and therefore should be high in order to achieve an efficient detector. This thesis will include absorption from both bound-to-bound and bound-to-continuum transitions, which are shown in figure 2.8.
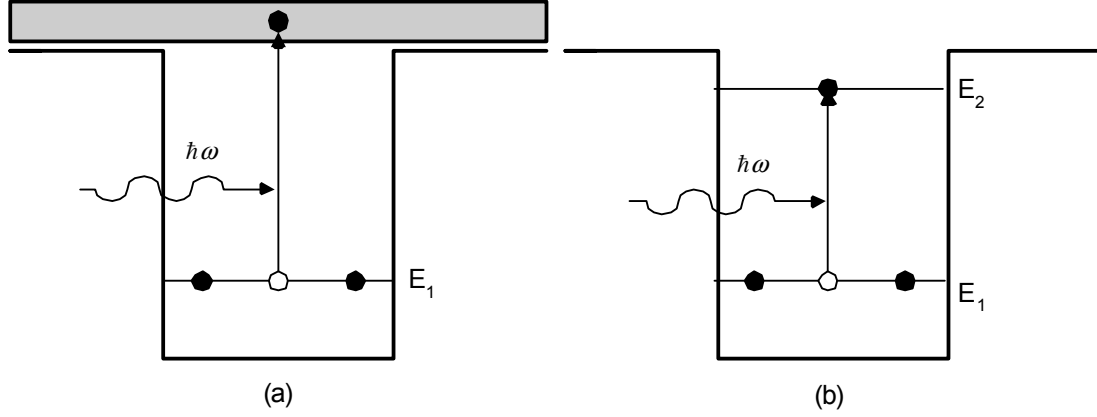
Figure 2.8   Diagram of (a) bound-to-continuum and (b) bound-to-bound transitions.

For the case of bound-to-bound transitions there is only one initial state and one final state, but there are $N = N_d LA$ electrons occupied in the initial state due to freedom of motion of the electrons in the xy plane, where N is the number of electrons in the initial state, N_d is the doping concentration in electrons per volume, L is the length of the well and A is the area of the well. Since all of these electrons have the same energy along the growth direction the sum in Equation (2.19) is over just one initial and final state multiplied by N. The delta function in Equation (2.19) can be approximated due to finite lifetime of the excited state by the normalized Lorentzian function given as (Yariv, 1997, pp. 162)

$$g(\hbar\omega) = \frac{1}{\pi} \frac{\left(\Gamma/2\right)}{\left(E_f - E_i - \hbar\omega\right)^2 + \left(\Gamma/2\right)^2} \tag{2.24}$$

where Γ is the full width half maximum value of the electron in the state E_f. Using the interaction potential from Equation (2.21) and the momentum operator

$$\mathbf{p} = -i\hbar\left(\partial/\partial x + \partial/\partial y + \partial/\partial z\right) \tag{2.25}$$

the transition rate can be found as

$$W_{B-B} = \frac{C_{B-B}}{\hbar\omega}(IAL)|< \psi_f | \frac{d}{dz} | \psi_i >|^2 \, g(\hbar\omega) \tag{2.26}$$

18

where $<\Psi_f | V_p | \Psi_i> \approx <\psi_f | V_p | \psi_i>$ for intersubband transitions and

$$C_{B-B} = \frac{N_d e^2 \hbar^3}{\left(m^*\right)^2 \varepsilon_0 n_r c}.$$

(2.27)

For the case of bound-to-continuum transitions there are still N initial states with energy E_i, but now there is also a continuum of final energy states and the summation over these final states amounts to replacing the delta function with the joint density of states $\rho(E_f)$, which is given by (Choi, 1997, pp. 131-133)

$$\rho(E_f) = \frac{1}{2\pi} \sqrt{\frac{2m_b^*}{\hbar^2 (E_f - V_b)}}$$

(2.28)

where m_b^* is the barrier effective mass and V_b is the barrier potential height. Therefore the transition rate for bound-to-continuum states is defined as

$$W_{B-C} = C_{B-C}(IAL) \sqrt{\frac{2m_b^*}{(\hbar\omega)^2 (E_f - V_b)}} |<\psi_f | \frac{d}{dz} | \psi_i>|^2$$

(2.29)

where

$$C_{B-C} = \frac{N_d e^2 \hbar^2}{2\left(m^*\right)^2 \varepsilon_0 n_r c}.$$

(2.30)

The absorption coefficient $\alpha(\hbar\omega)$ is defined as

$$\alpha(\hbar\omega) = \frac{\text{number of transitions per unit volume and time}}{\text{incident photon flux}} = \frac{\left(W/_{AL}\right)}{I}$$

(2.31)

and the absorption coefficient for both bound-to-bound and bound-to-continuum transitions can be derived.

$$\alpha_{B-B}(\hbar\omega) = \frac{C_{B-B}}{\hbar\omega} |<\psi_f | \frac{d}{dz} | \psi_i>|^2 g(\hbar\omega)$$

(2.32)

$$\alpha_{B-C}(\hbar\omega) = C_{B-C} \sqrt{\frac{2m_b^*}{(\hbar\omega)^2 (E_f - V_b)}} |<\psi_f | \frac{d}{dz} | \psi_i>|^2$$

19

An example of the absorption coefficient for bound-to-bound and bound-to-continuum transitions is shown in figures 2.9 and 2.10. The sharp peak in figure 2.9 results from the bound-to-bound transitions occurring whenever the incident photon has energy equal to $E_2 - E_1$, whereas the shape of the absorption curve in figure 2.10 is relatively broad due to the continuum of energies above the well. The amplitude of the bound-to-continuum absorption coefficient decreases as the photon energy increases because the density of states decreases the further above the well you go.
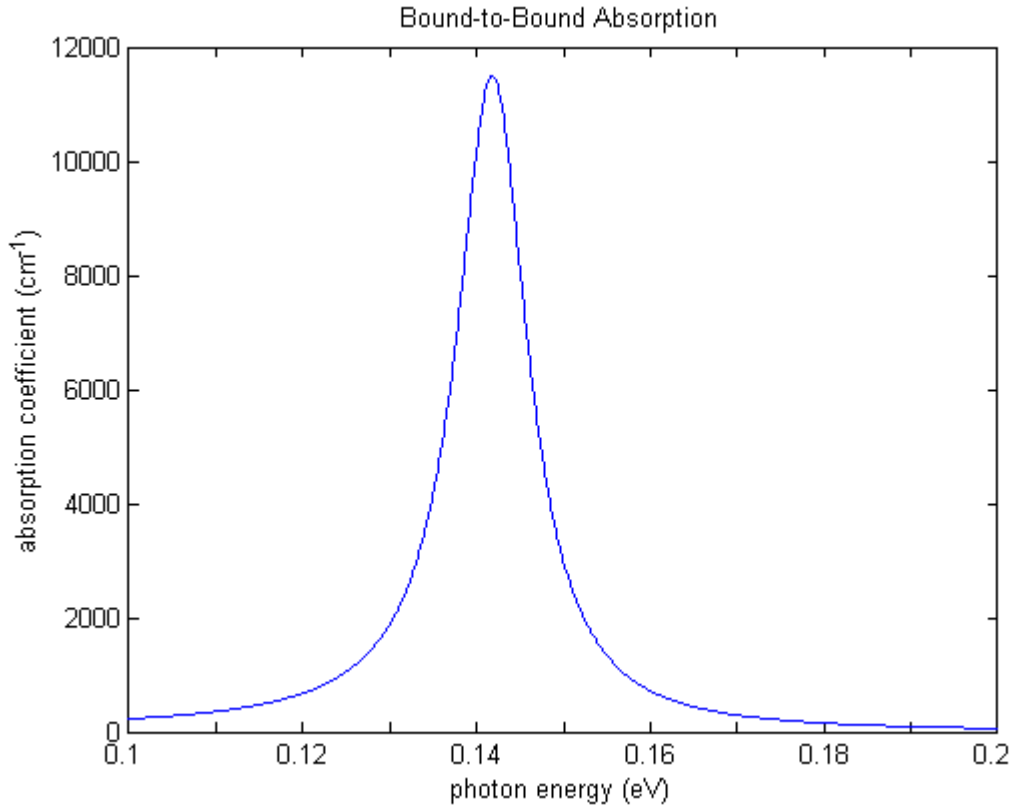
Figure 2.9   Bound-to-bound absorption curve for $(In_{0.53}Ga_{0.47}As)_{0.15}(InP)_{0.85}/$ $In_{0.53}Ga_{0.47}As /(In_{0.53}Ga_{0.47}As)_{0.45}(InP)_{0.55}$ with a=25 Å and b=44 Å with no external bias and $\Gamma = 10\ meV$.
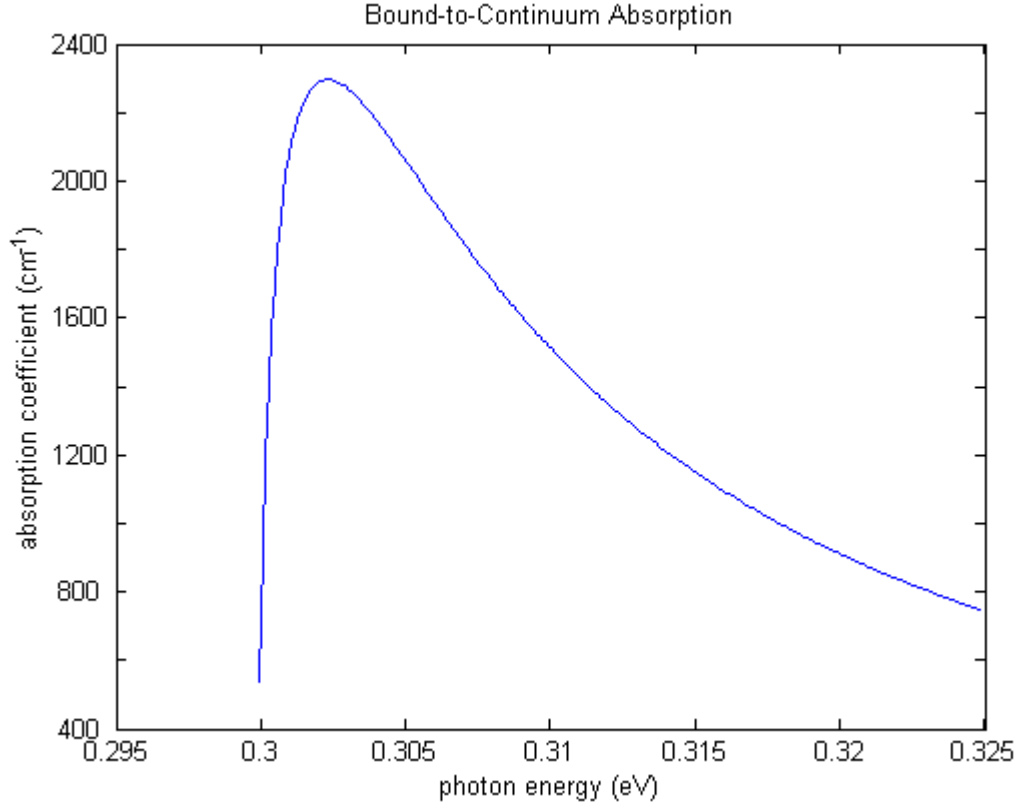
Figure 2.10   Bound-to-continuum absorption curve for the quantum well in Figure 2.9 with no external bias.

E.   SUMMARY

In this chapter the transfer matrix method was developed and used to calculate the energy levels and wavefunctions in a quantum well. Selection rules for interband and intersubband transitions and their importance in detector design were discussed and the absorption coefficient for both bound-to-bound and bound-to-continuum transitions was derived theoretically using Fermi's golden rule (2.19). In the next chapter, we will discuss some of the design aspects that are considered when designing a multicolor QWIP and how the addition of an external bias will effect these considerations.

THIS PAGE INTENTIONALLY LEFT BLANK

III. DESIGN OF A QW STRUCTURE FOR INFRARED DETECTION

A.   INTRODUCTION

As discussed in Chapter II, surrounding a low-bandgap material with a high-bandgap material will form a quantum well. The choice of which materials to use is important as it will affect the transition wavelengths as well as the absorption coefficient, and therefore the efficiency of the detector. Some of the factors to consider in the choice of materials to use are bandgap, lattice constant, and what wavelengths are to be detected. During this thesis multiple materials were tried in order to optimize the structure so that it would detect a wavelength of 1.06 μm and a wavelength of 8-10 μm. No matter which materials were used in the structure, their bandgaps and effective masses were determined by Vegard's Law with a bowing parameter to take into account non-uniformities of alloying (Singh, 1993, pp. 185).

$$E_g^{A_xB_{1-x}} = xE_g^A + (1-x)E_g^B + x(1-x)C_{AB}$$

$$\frac{1}{m_{A_xB_{1-x}}^*} = \left(\frac{x}{m_A^*} + \frac{1-x}{m_B^*} \right)$$

(3.1)

where x is the molar percentage of material A and C_{AB} is the experimentally determined bowing parameter. An example of how the composite energy gaps, at the Γ-point, and relative effective masses change with molar percentage is shown in Figures 3.1 and 3.2 where the energy gaps and effective masses for each material are given in Table 3.1 (Note that the bowing parameter is not considered in these cases).

23

Material	Energy Gap (eV)	Relative effective mass $\left(m^*/m_e\right)$
AlAs	2.671	0.15
GaAs	1.424	0.067
InAs	0.36	0.028

Table 3.1   Energy gap and relative effective mass values for specific materials. From: Singh, 1993, pp. 184-185
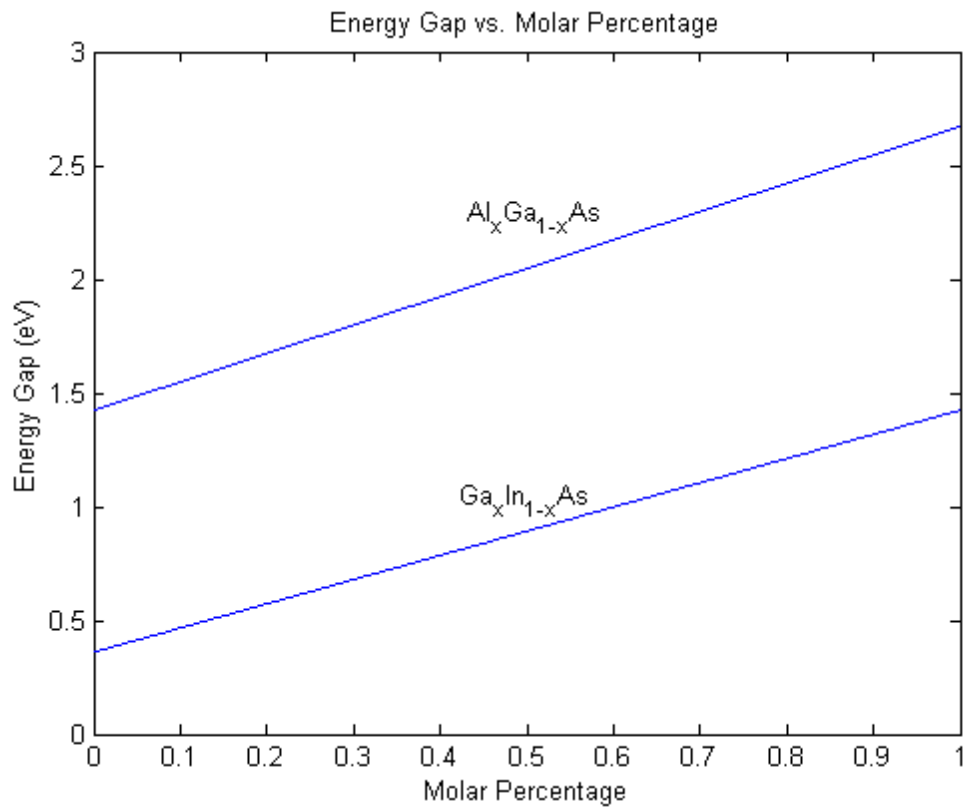
Figure 3.1   Diagram of Energy Gap vs. Molar percentage for $Al_xGa_{1-x}As$ and $Ga_xIn_{1-x}As$ at the Γ-point.
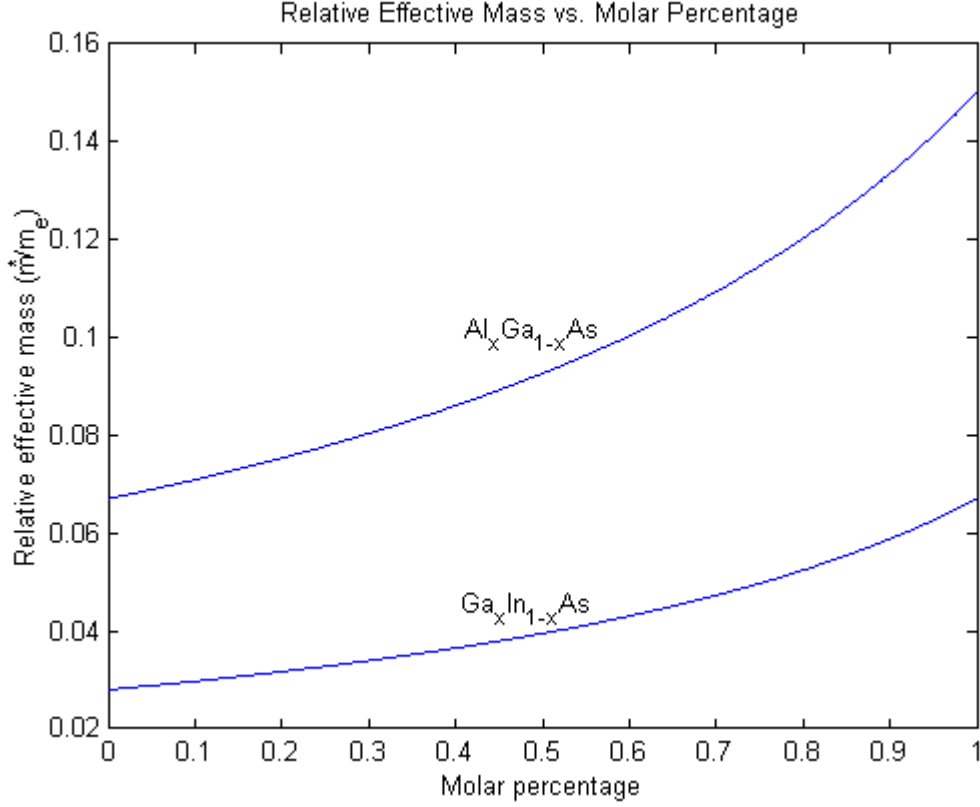
Figure 3.2   Diagram of Relative effective mass vs. Molar percentage for
$Al_xGa_{1-x}As$ and $Ga_xIn_{1-x}As$

The potential heights in the conduction and valence band depend on the difference
in energy gaps between two regions and are not the same, as might be expected, but differ
so that the conduction band potential height is larger than the valence band. This
difference is difficult to predict theoretically and can only be determined for each
material experimentally, however, when modeling a quantum well structure it is assumed
that to a good approximation the potential heights in the conduction and valence bands is
given as

$$V_C = 0.6\left(E_g^{A_xB_{1-x}} - E_g^{A_yB_{1-y}} \right)$$

$$V_V = 0.4\left(E_g^{A_xB_{1-x}} - E_g^{A_yB_{1-y}} \right)$$

(3.2)

In early QWIP research, studies focused on quantum well structures that utilized
bound-to-bound transitions (Levine *et al.* 1987). In a bound-to-bound QWIP the

electrons in the lowest state are excited by incoming photons into the excited state and then tunnel through the barrier under an external bias to form a photocurrent as is shown in figure 3.3.
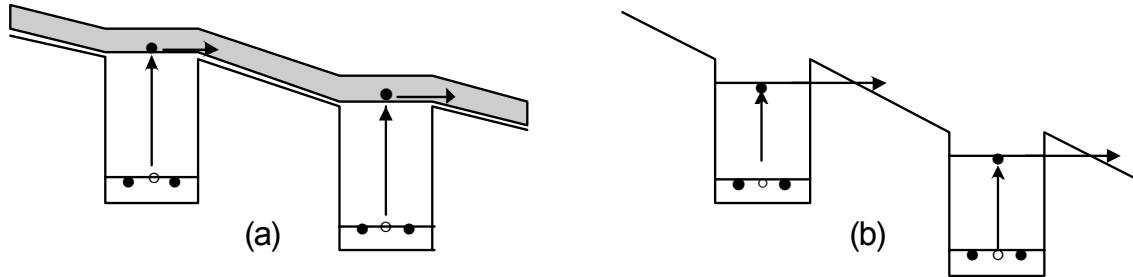
Figure 3.3   Schematic Diagram showing (a) bound-to-continuum and (b) bound-to-bound electron transport.

The barrier thickness was designed to be large enough to prevent tunneling from the lowest state (typically about 500 Å); however, this barrier thickness reduced the photoresponse due to the reduction in tunneling probability of the photoelectrons. Another problem with these early designs was that the photoresponse spectrum was relatively narrow due to there being only two states and was not practical for infrared imaging.   These problems ushered in the second generation of QWIPs, which used bound-to-continuum transitions (Hasnain *et al.*, 1989).   In these structures, electrons in the ground state are excited into the continuum where they contribute to the photocurrent without tunneling (Figure 3.3) and therefore the barrier thickness has less bearing on the photocurrent. Due to the continuum of states and the multiple transitions that can occur, the photoresponse spectrum was much wider than in the bound-to-bound design, but the absorption coefficient was much smaller due to the low density of states above the well. It is easy to see that there is a trade-off between having good transport of photoelectrons and strong absorption and that both are important in the design of a QWIP.   In the following sections, these factors will be used to motivate the design of a quantum well structure for two-color infrared detection.

B. STEP QUANTUM WELL STRUCTURE FOR DUAL COLOR DETECTION

In the past, attempts have been made to detect multiple "colors", or wavelengths, with an infrared imager by using square quantum wells (Köck *et al.*, 1992, Gravé *et al.*, 1992, Liu *et al.*, 1993), but as was shown in section 2.3, transition selection rules prohibit the transition from the first valence level to the second conduction level and therefore that wavelength cannot be detected. This implies that only one wavelength of light can be detected with a square quantum well. One method used to detect more than one wavelength of light using square quantum wells was to stack multiple wells on top of each other and hold each well responsible for detecting one specific wavelength of light (Köck *et al.*, 1992, Gravé *et al.*, 1992, Liu *et al.*, 1993). This type of structure is easy to design, but very difficult to fabricate due to the need for multiple contacts at each well. Recently researchers have been exploring the use of asymmetric, or step, quantum wells (Ting *et al.*, 1997) to detect multiple wavelengths.

In a step quantum well, the symmetry of the wavefunctions is broken and transitions that were forbidden in a square quantum well can occur. For this thesis, the optimized design of the step quantum well is to have two energy levels in the conduction band, one above and below the step, which account for the middle infrared wavelength, and one energy level in the valence band, below the step, that accounts for the 1.06 μm transition as illustrated in figure 3.4. The second energy level in the conduction band is designed to be as near the top of the quantum well as possible in order to get a good photocurrent with very little bias.
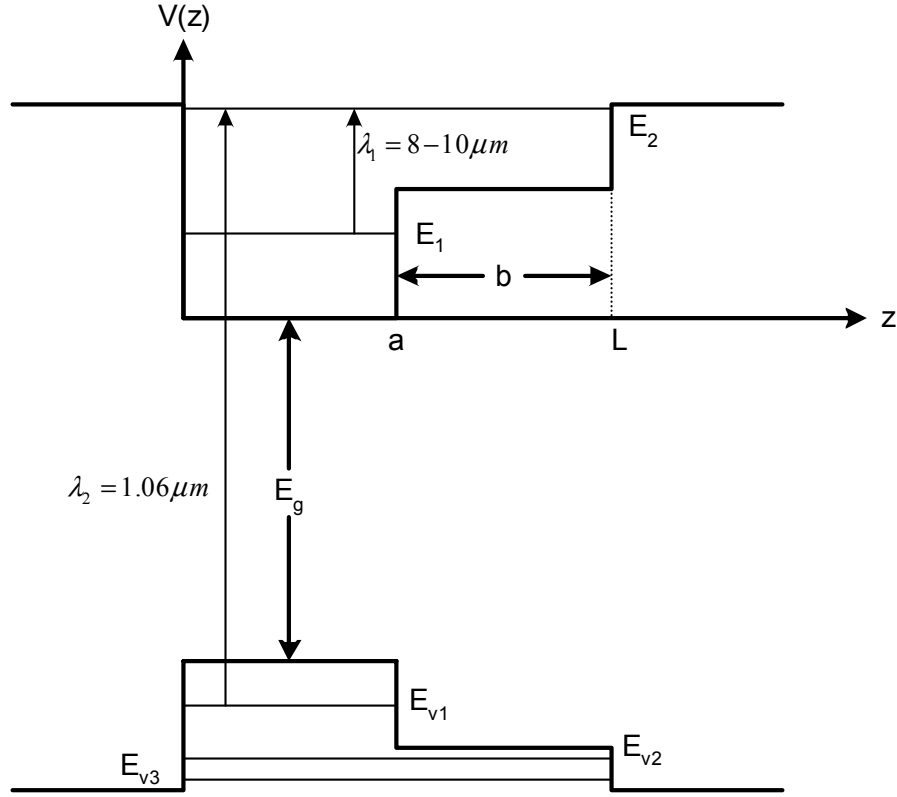
Figure 3.4   Schematic diagram of the ideal quantum well for this thesis.

The application of the bias will cause the quantum well to "slant" and will force the second energy level into the continuum allowing the photoexcited electrons to be extracted without tunneling through the barrier. The energy levels will be affected by the bias and therefore the peak detection wavelengths will shift. The asymmetry of the quantum well will give rise to a linear Stark shift which is approximately given by $\dfrac{eFb}{2}$ where e is the electron charge, F is the applied electric field in volts per meter and b is the length of the step in the quantum well. The accurate shift in detection wavelength is important in the design since it is necessary to apply an external bias to a device in order to extract the photocurrent. Due to the necessity of using an external bias it becomes important to be able to model how the peak detection wavelengths will change in order to optimize the QWIP structure, in particular for the 1.06 μm wavelength. The next section will introduce a transfer matrix method for a quantum well under a bias and this method will be used to model the change in transition wavelengths due to an external bias.

C. TRANSFER MATRIX METHOD UNDER AN APPLIED BIAS

When a quantum well structure is subjected to an applied bias the potential well will tilt in the direction opposite the electric field and therefore the potential of an electron in the quantum well is given as

$$V(z) = V_n - eFz \qquad (3.3)$$

where V_n is the potential height of the well, e is the electron charge, F is the applied electric field in volts per meter and z is the direction of growth. An example of the effect of an external bias on a square quantum well structure is shown in Figure 3.5
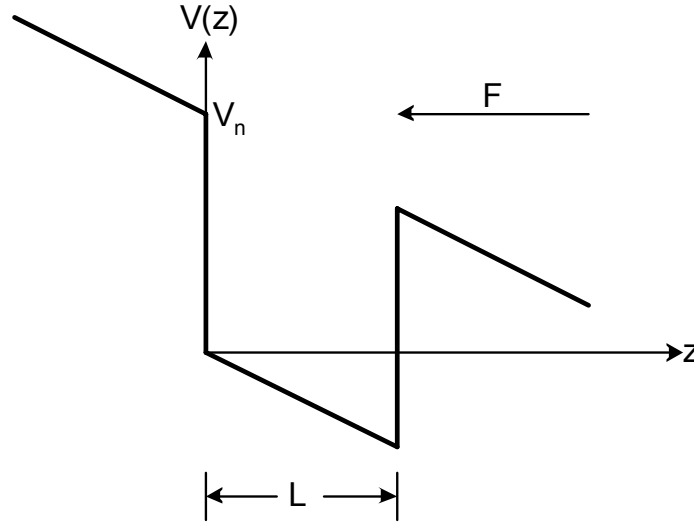
Figure 3.5   Diagram of a square quantum well under an external bias.

Substituting Equation (3.3) into the Schrödinger equation

$$\left(-\frac{\hbar^2}{2m_n^*}\frac{\partial^2}{\partial z^2} + V(z) \right)\psi_n(z) = E_n\psi_n(z) \qquad (3.4)$$

the following formula can be derived

$$\frac{\partial^2\psi_n(z)}{\partial z^2} = \frac{2m_n^*e}{\hbar^2}(-Fz - \eta_n)\psi_n(z) \qquad (3.5)$$

where

$$\eta_n = \frac{E - V_n}{e} \tag{3.6}$$

and where V_n is the potential height in the nth region. Equation (3.5) can further be simplified using the following coordinate transformation

$$\rho_n(z) = \frac{-Fz - \eta_n}{\beta} \tag{3.7}$$

and the result is of the form of the Airy differential equation

$$\frac{\partial^2 \psi_n(z)}{\partial \rho_n(z)^2} = \rho_n(z)\psi_n(z) \tag{3.8}$$

with

$$\beta = \left(\frac{\hbar^2 F^2}{2m_n^* e} \right)^{\frac{1}{3}}. \tag{3.9}$$

The solution to Equation (3.8) is a linear combination of Airy functions given as (Vatannia *et al.*, 1996)

$$\psi_n(z) = A_n Ai(\rho_n(z)) + B_n Bi(\rho_n(z)) \tag{3.10}$$

where *Ai* and *Bi* are Airy functions of the first and second kind, respectively. By substituting Equation (3.10) into the boundary conditions given by Equation (2.7) a relationship can be developed between the coefficients of the wavefunctions in each region.

$$\begin{bmatrix} A_n \\ B_n \end{bmatrix} = \mathbf{M_n} \begin{bmatrix} A_{n+1} \\ B_{n+1} \end{bmatrix} \text{ for } n = 1, 2, 3, ... N - 1 \tag{3.11}$$

Furthermore, a relationship can be developed between the coefficients in the first and last region.

$$\begin{bmatrix} A_1 \\ B_1 \end{bmatrix} = \mathbf{M_1 M_2 M_3 ... M_{N-1}} \begin{bmatrix} A_N \\ B_N \end{bmatrix} = \mathbf{M} \begin{bmatrix} A_N \\ B_N \end{bmatrix} = \begin{bmatrix} m_{11} & m_{12} \\ m_{21} & m_{22} \end{bmatrix} \begin{bmatrix} A_N \\ B_N \end{bmatrix} \tag{3.12}$$

30

where

$$\mathbf{M_n} = \pi \begin{pmatrix} Ai(\alpha_{n+1})Bi'(\alpha_n) - \sigma_n Ai'(\alpha_{n+1})Bi(\alpha_n) & Bi(\alpha_{n+1})Bi'(\alpha_n) - \sigma_n Bi(\alpha_n)Bi'(\alpha_{n+1}) \\ \sigma_n Ai(\alpha_n)Ai'(\alpha_{n+1}) - Ai'(\alpha_n)Ai(\alpha_{n+1}) & \sigma_n Ai(\alpha_n)Bi'(\alpha_{n+1}) - Ai'(\alpha_n)Bi(\alpha_{n+1}) \end{pmatrix} \quad (3.13)$$

and

$$\alpha_n = \left(\frac{2m_n^* eF}{\hbar^2} \right)^{1/3} (-z_n - \eta_n) = \gamma_n(-z_n - \eta_n)$$

$$\alpha_{n+1} = \left(\frac{2m_{n+1}^* eF}{\hbar^2} \right)^{1/3} (-z_n - \eta_{n+1}) = \gamma_{n+1}(-z_n - \eta_{n+1})$$

$$(3.14)$$

$$\sigma_n = \left(\frac{m_n^* \gamma_{n+1}}{m_{n+1}^* \gamma_n} \right). \quad (3.15)$$

The primes in Equation (3.13) represent the derivatives of the Airy functions and the factor of π comes from the fact that $\left(Ai(\alpha_n)Bi'(\alpha_n) - Ai'(\alpha_n)Bi(\alpha_n) \right) = \frac{1}{\pi}$. In the case of bound states, the wavefunctions must decay to zero as $z \rightarrow \pm\infty$. This constraint forces $B_1 = 0$ since the second order Airy function, $Bi(\alpha_n)$, tends to ∞ as $z \rightarrow -\infty$. Similarly, $A_N = 0$ since $Ai(\alpha_n)$ tends to ∞ as $z \rightarrow \infty$. These conditions cause Equation (3.12) to take the form

$$\begin{bmatrix} A_1 \\ 0 \end{bmatrix} = \begin{bmatrix} m_{11} & m_{12} \\ m_{21} & m_{22} \end{bmatrix} \begin{bmatrix} 0 \\ B_N \end{bmatrix} \quad (3.16)$$

and, just like the derivation of the unbiased transfer matrix method, the requirement for eigen states is

$$m_{22}(E) = 0. \quad (3.17)$$

We wrote a program to find and plot $m_{22}(E)$ versus E and find the energy levels when Equation (3.17) is satisfied. Figure 3.6 shows $m_{22}(E)$ as a function of energy and figure 3.7 shows the calculated energy levels and wavefunctions for the conduction band of a

31

step quantum well under an external bias. The parameters of the quantum well were taken from a previously published work (Karunasiri *et al.*, 1990) so that the results found using this program could be compared with experimental data.
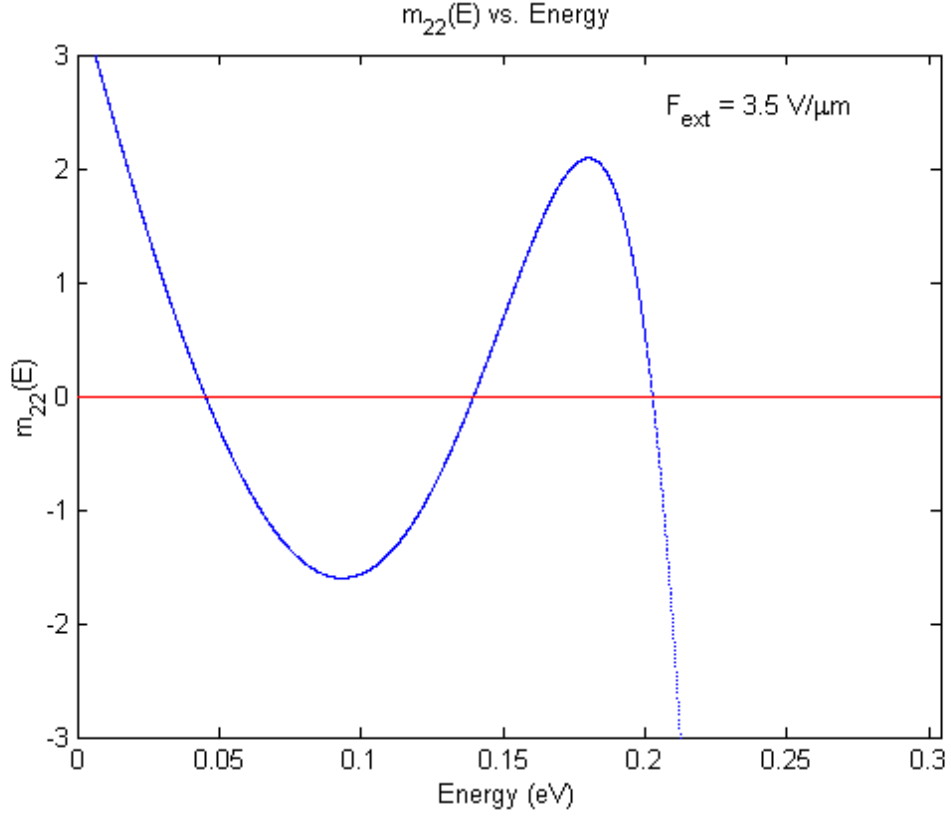
Figure 3.6   Plot of $m_{22}(E)$ vs. E for $Al_{0.44}Ga_{0.56}As/GaAs/Al_{0.18}Ga_{0.82}As$ well with a=60 Å and b=90 Å and an external electric field, $F_{ext} = 3.5 V/\mu m$.
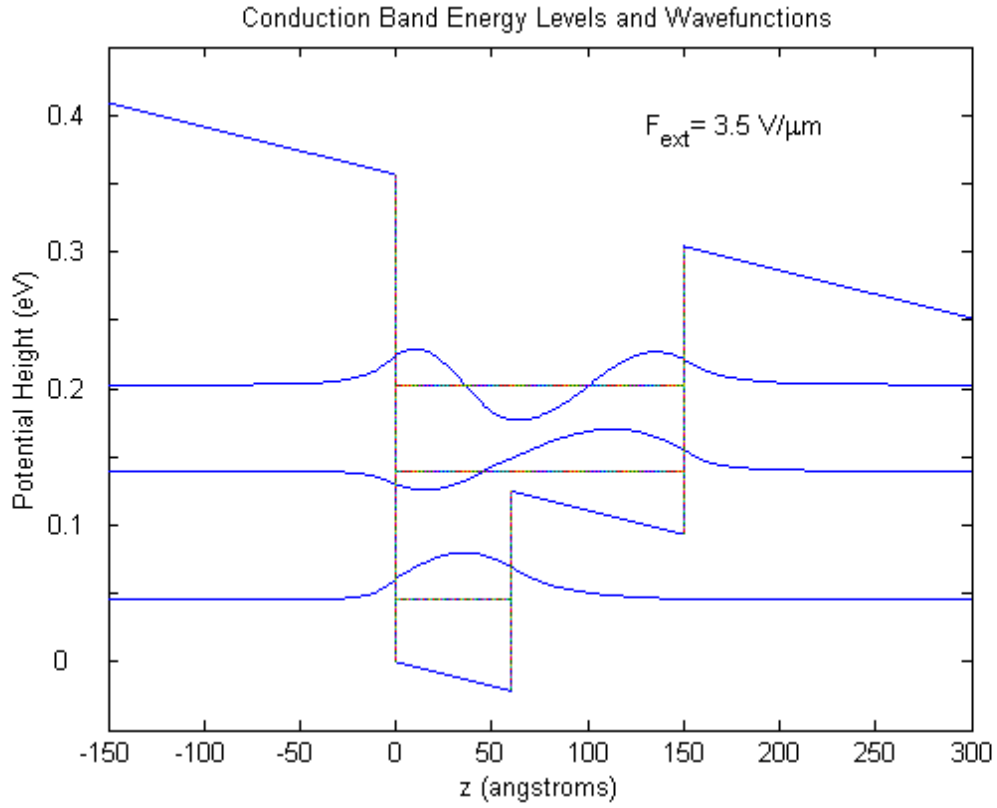
Figure 3.7   The first three conduction band energy levels and wavefunctions of the
quantum well in figure 3.6.

The eigen states and wavefunctions of the step well formed in the valence band
can be obtained using the same approach as above with corresponding potential heights
and effective masses. Figure 3.8 shows the calculated energy levels and wavefunctions
in the valence band for heavy holes.
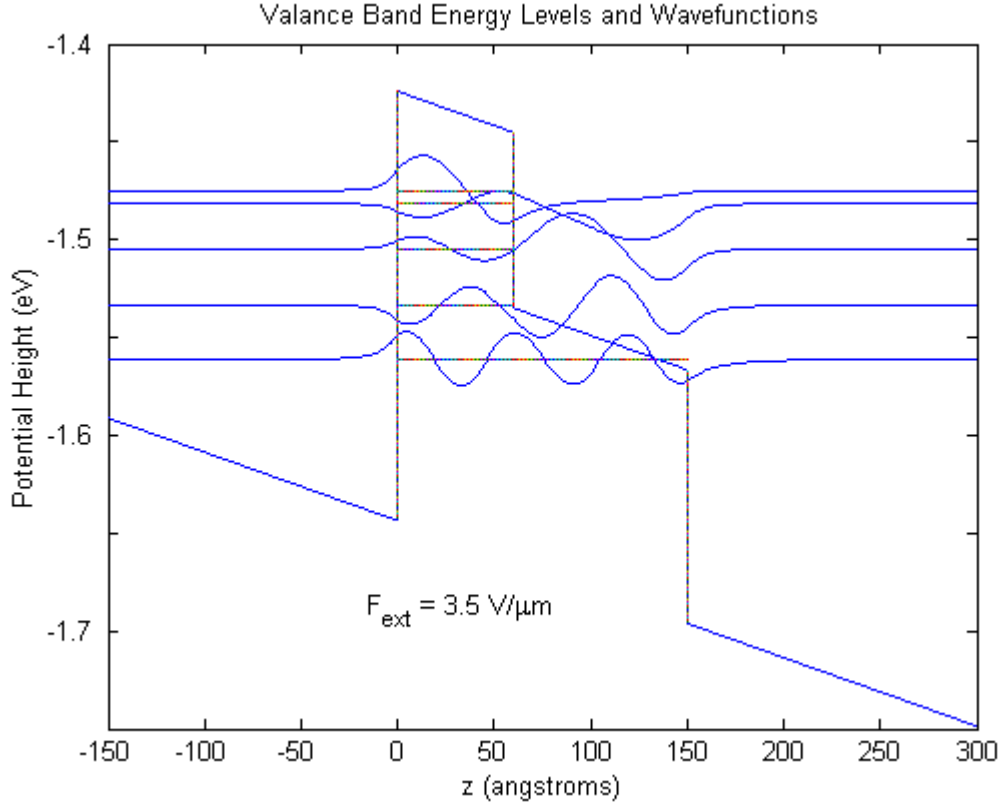
Figure 3.8   Valence band energies and wavefunctions for the step well in Figure 3.6.

The introduction of the external bias will cause a shift in the energy levels of the asymmetric quantum well and therefore, the absorption coefficient defined by Equation (2.32) will also change. For the QWIP design used in this thesis, the addition of the bias will force the excited state, which was very near the top of the well, into the continuum so that only the bound-to-continuum absorption coefficient is considered when a bias is introduced. Figure 3.9 demonstrates how the external bias will affect the peak detection wavelength.
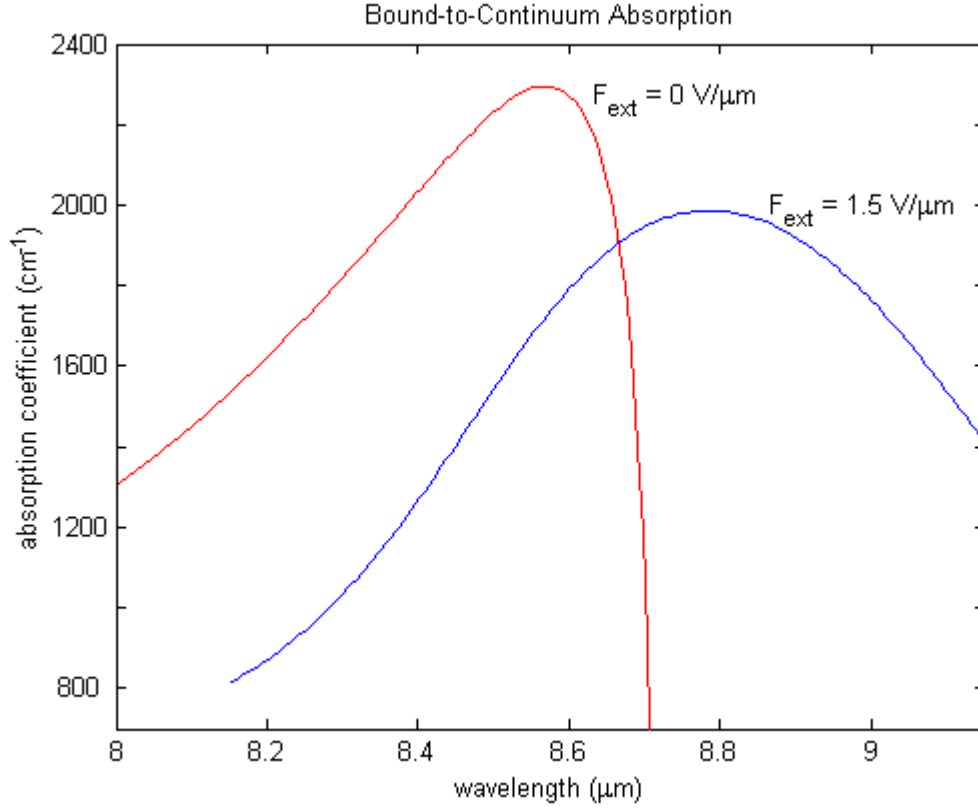
Figure 3.9   Plot of the bound-to-continuum absorption vs. wavelength for the $(In_{0.53}Ga_{0.47}As)_{0.15}(InP)_{0.85} / In_{0.53}Ga_{0.47}As /(In_{0.53}Ga_{0.47}As)_{0.55}(InP)_{0.45}$ well with a = 25 Å and b = 44 Å and with a bias of 0 V/µm and 1.5 V/µm.

This section has introduced a transfer matrix method for a quantum well structure under an external bias. This method was used to calculate the energy levels, wavefunctions and absorption coefficient for a quantum well, which is useful in optimizing detector design. The next section will compare the output of the computer model designed in this thesis with experimental data in order to tell the accuracy of the computer model.

D.   COMPARISON WITH EXPERIMENTAL DATA

The quantum well structure that the computer model was compared to came from a paper written by Karunasiri *et al.* (1990). This paper utilized a $Al_{0.44}Ga_{0.56}As / GaAs / Al_{0.18}Ga_{0.82}As$ step quantum well with a = 60 Å and b = 90 Å. This structure has four energy levels in its conduction band, but the paper focused on the

bound-to-bound absorption from the 1-2 and 1-3 transitions due to the minute absorption strength of the 1-4 transition. Figure 3.10 shows the energy levels of the conduction band and Table 3.2 shows the effective masses and energy gaps used in the computer model.

Energy Levels of the Asymmetric Quantum Well
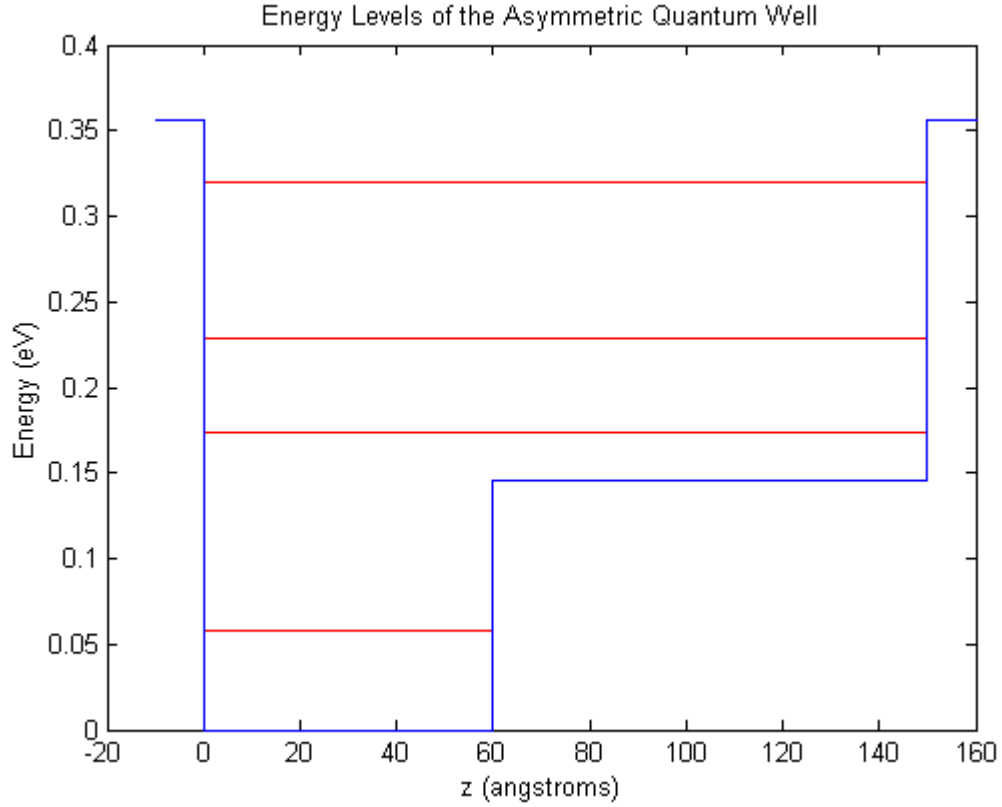
Figure 3.10   Energy levels of the $Al_{0.44}Ga_{0.56}As / GaAs / Al_{0.18}Ga_{0.82}As$ well with a = 60Å and b = 90Å.

Layer	m^* (kg)	E_g (eV)
Al$_{0.44}$Ga$_{0.56}$As	$0.1082\, m_e$	1.9727
GaAs	$0.067\, m_e$	1.424
Al$_{0.18}$Ga$_{0.82}$As	$0.0794\, m_e$	1.6485

Table 3.2   Parameters used in the quantum well in Figure 3.10

Since this is a step quantum well all energy transitions are allowed and only the bound-to-bound absorption is considered in this analysis to compare with the experimental data. Figure 3.11 shows the calculated absorption coefficient for the 1-2 and 2-3 energy transitions under both positive and negative external bias.

36
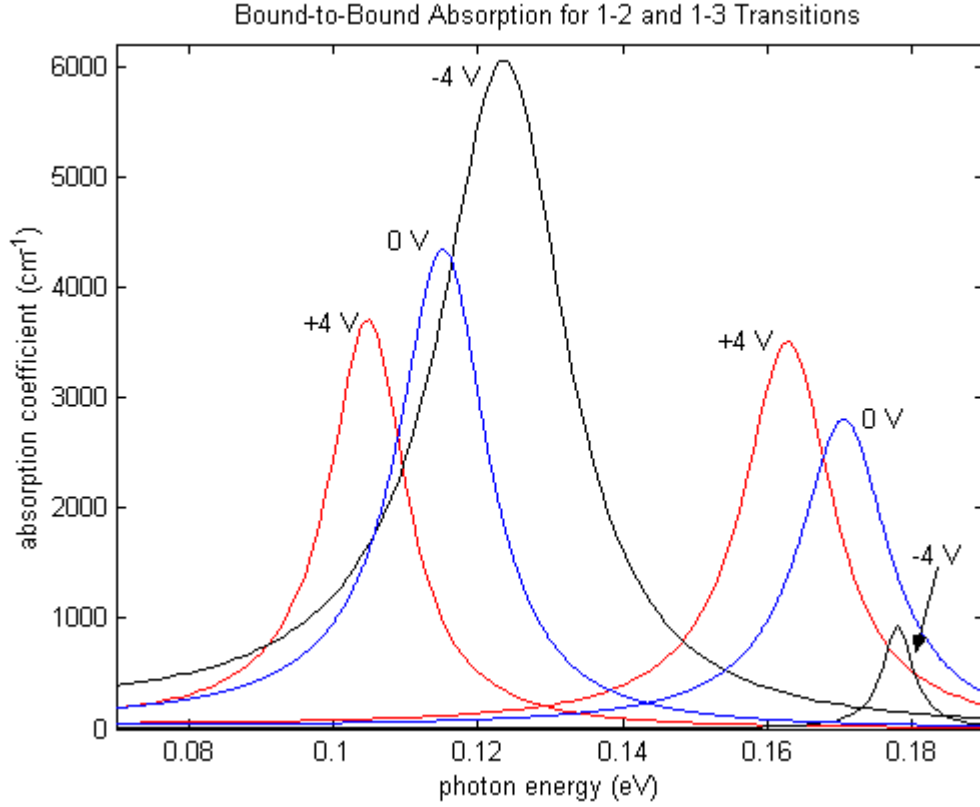
Figure 3.11   Bound-to-bound absorption curves for 1-2 and 1-3 transitions of the quantum well in Figure 4.6 with $\Gamma=15meV$.

Since the experimental data is measured in absorbance, the absorption coefficient is converted to absorbance using the following relation

$$Absorbance = x(\log e)\alpha(\hbar\omega) = W(\sin^2(17°))(\log e)\alpha(\hbar\omega)$$
$$= (2.56*10^{-6}cm)(\log e)\alpha(\hbar\omega)$$

(3.18)

where W is the width of the absorbing material and the $\sin^2(17°)$ term comes from the polarization of the light hitting the device at the Brewster angle ($\theta = 73°$). Using this equation the absorbance can be found for both transitions and is shown in Figure 3.12.
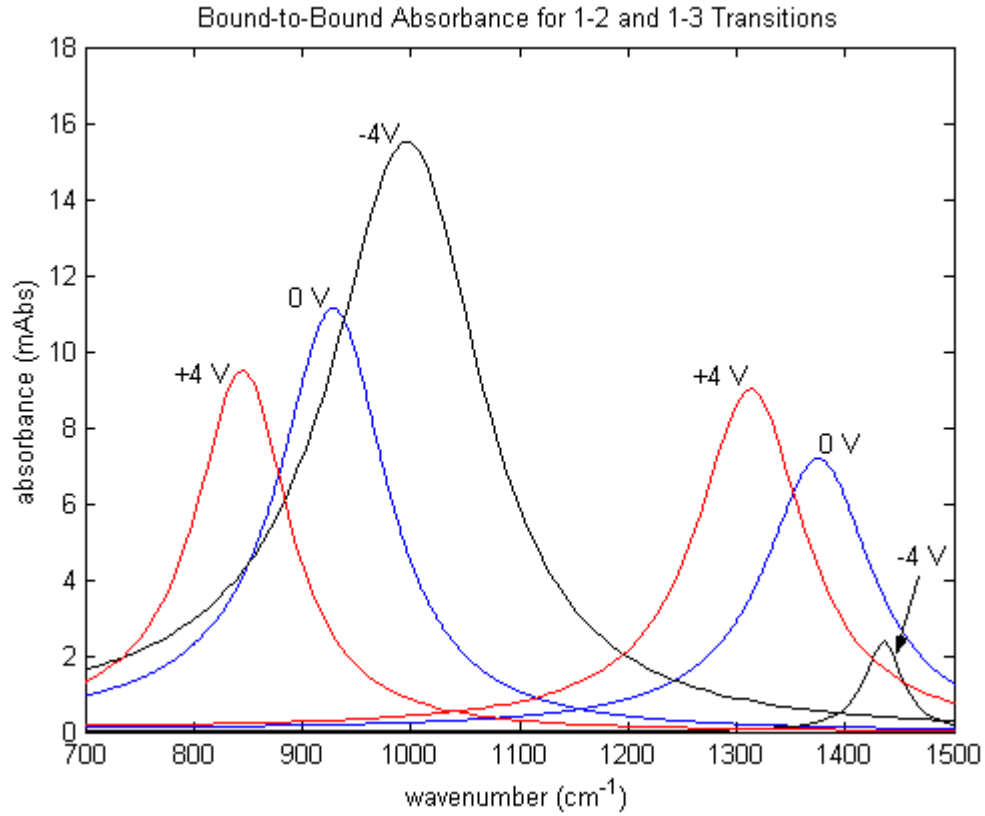
Figure 3.12   Bound-to-bound absorbance curves for 1-2 and 1-3 transitions of the quantum well in Figure 4.6 with $\Gamma = 15 meV$.

This Figure can be compared with the absorbance curves obtained experimentally, which is shown in Figure 3.13 (Note that the absorbance data in the Figure is plotted in decreasing order of wavenumber).
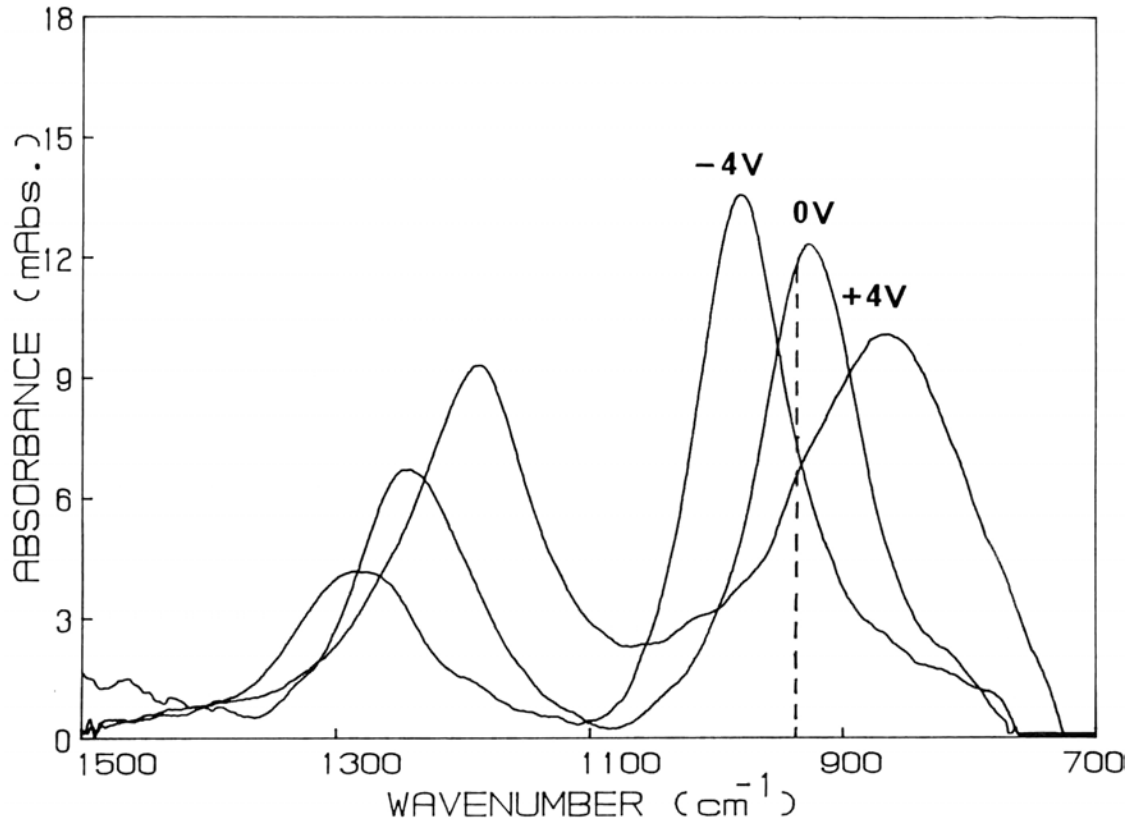
Figure 3.13   Bound-to-bound absorbance curves obtained experimentally using the
quantum well in Figure 4.6. From: Karunasiri *et al.*, 1990.

Comparing Figures 3.12 and 3.13 it can easily be seen that the values for the absorbance obtained from our model and those obtained experimentally are very close and that the computer model used in this thesis is a good approximation to the real world.

E.   SUMMARY

This chapter introduced some of the parameters that affect the design of a QWIP and a method for detecting multiple infrared wavelengths using an asymmetric quantum well design. The optimum design characteristics used in this thesis were also presented along with a motivation for modeling the effects of an external bias on a quantum well structure. A transfer matrix method utilizing Airy functions was derived to model the effects of an external bias and this method was used to show how the peak detection wavelength shifts due to the bias. The data obtained using our computer model was then compared to experimental data and shown to be a good approximation to real life,

granting greater confidence in any information obtained using the model. The next chapter introduces the optimum design of the QWIP structure used in this thesis along with an analysis of how it will react to an external bias.

IV.   DESIGN PARAMETERS OF THE TWO-COLOR DETECTOR

A.   INTRODUCTION

As was mentioned in chapter III, many different material systems were considered in designing the asymmetric well used in this thesis.   At first, a $Al_xGa_{1-x}As/GaAs/Al_yGa_{1-y}As$ step well was considered due to the abundance of experimental data on these two materials and because they are lattice matched, which would make them much easier to grow. This structure could be designed to detect the middle infrared wavelength (MIRW), but could not detect the 1.06 μm wavelength due to its large bandgap. This prompted the use of materials with smaller bandgaps, which could be identified by using Figure 4.1 (Tu *et al.*, 1992, pp. 158).
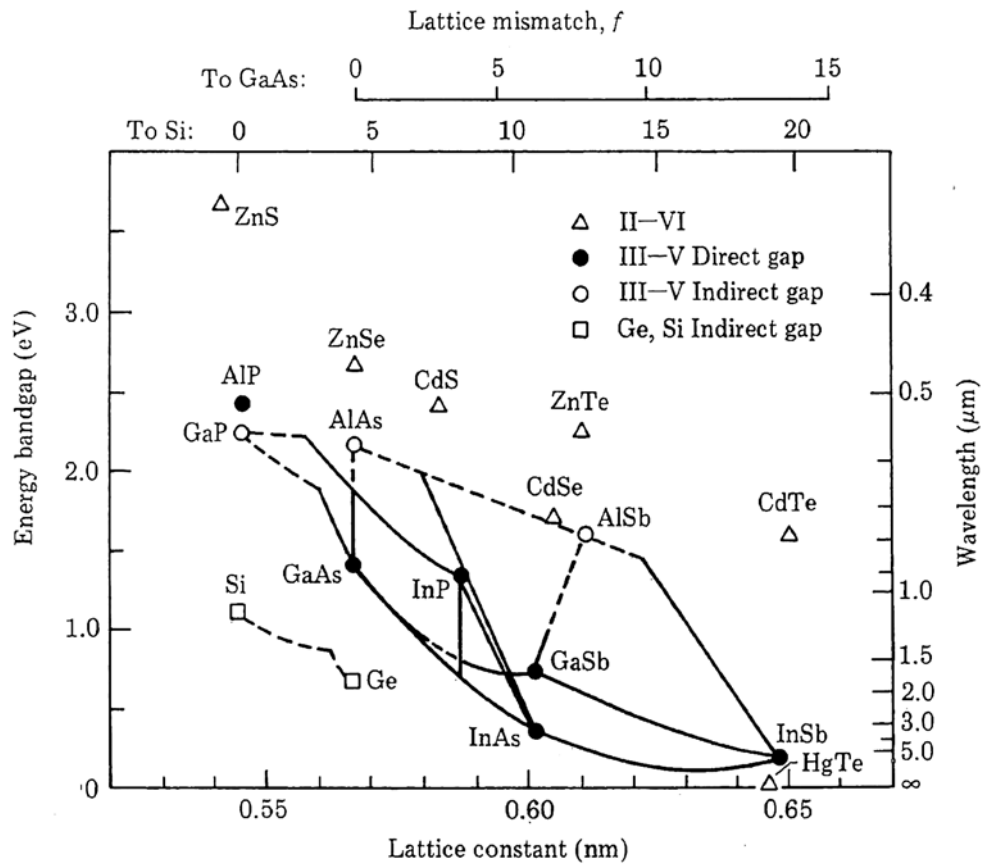
Figure 4.1   Diagram of bandgap vs. Lattice constant for different materials.

The next *GaAs*-based quantum well design that was tried consisted of $GaAs / In_xGa_{1-x}As / In_yGa_{1-y}As$ and could be designed to detect both the MIRW and 1.06 μm wavelengths, but not at the same time. The reason that both wavelengths could not be detected at the same time using these materials was that in order to detect the 1.06 μm wavelength the energy gaps had to be widened, but this caused the two conduction band energy levels to become closely spaced, which pushed the MIRW outside of the 8-10 μm design window. Another problem with the design of this quantum well was that if the molar percentage of Indium became large there was a significant lattice mismatch between the two materials, which would introduce dislocations into the sample. In order to lessen the lattice mismatch, a quantum well consisting of $InP / In_xGa_{1-x}As / In_yGa_{1-y}As$ was designed because the energy gap of InP and GaAs are about the same and because the two materials have much closer lattice constants to provide for easier growth. This quantum well structure could also be designed to detect the MIRW and 1.06 μm wavelengths, but the problem remained that both wavelengths could not be detected at the same time because the energy gap of InP was still too large. Following Figure 4.1 this left only one choice of possible materials for the final design: the quaternary *InGaAsP* and $In_{0.53}Ga_{0.47}As$. These materials provided the advantage of being lattice-matched and also by varying the amount of *InP* in the quaternary the bandgap could be brought down to the point where both wavelengths could be detected. The following section will discuss the quantum well that was designed using these materials and will show the theoretical results for the absorption with and without an external bias.

B.   OPTIMUM QUANTUM WELL DESIGN

One of the problems with using the quaternary material in the design of the quantum well was that very little experimental data was readily available and no theoretical data could be found. However, a paper written by Vurgaftman *et al.* (2001) provided all of the necessary experimental data not only for the quaternary material, but also for every other material that was used throughout this thesis. Using the values from

this paper, an optimized quantum well was designed with the following layer structure:
$(In_{0.53}Ga_{0.47}As)_{0.15}(InP)_{0.85} / In_{0.53}Ga_{0.47}As /(In_{0.53}Ga_{0.47}As)_{0.55}(InP)_{0.45}$ with a thickness of
the well of 25 Å and of the step of 44 Å. Figure 4.2 shows the optimized quantum well
structure, energy levels, and transition wavelengths and Table 4.1 shows the values of the
effective masses and energy gaps in each layer of the optimum design.
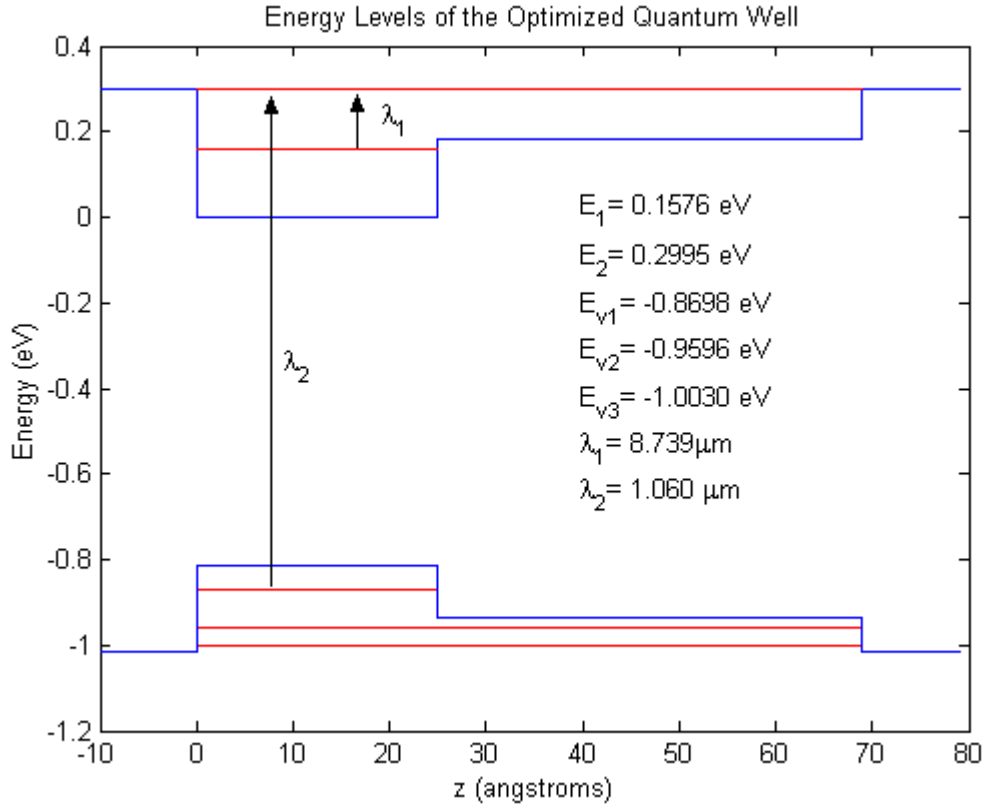
Figure 4.2   Optimized quantum well structure and energy levels with no external bias.

Layer	m^* (kg)	m^*_{hh} (kg)	E_g (eV)
(In₀.₅₃Ga₀.₄₇As)₀.₁₅(InP)₀.₈₅	$0.0676\,m_e$	$0.4905\,m_e$	1.3159
In₀.₅₃Ga₀.₄₇As	$0.0365\,m_e$	$0.3403\,m_e$	0.8161
(In₀.₅₃Ga₀.₄₇As)₀.₅₅(InP)₀.₄₅	$0.0519\,m_e$	$0.4242\,m_e$	1.1181

Table 4.1   Parameters used to design the final quantum well structure used in this
thesis. m^*_{hh} is the heavy-hole effective mass and m_e is the electron mass.

It is important to mention that the values for the energy gaps found in Table 4.1 are the
values when the temperature, $T = 0K$. The reason for choosing these values over the

43

room temperature ($T = 290K$) values is that in order to limit the dark current of the device under operating conditions it must be cooled down to $T \leq 77K$. The difference in the energy gaps and the energy levels of this structure at $T = 0K$ and $T = 77K$ is small so that for design purposes it was assumed that the device is operating at $T = 0K$. Figures 4.3 and 4.4 show the effects of external bias on the quantum well structure and energy levels.

Energy Levels of the Optimized Quantum Well

$F_{ext} = 1.5$ V/μm

$E_1 = 0.1553$ eV

$E_{v1} = -0.8624$ eV
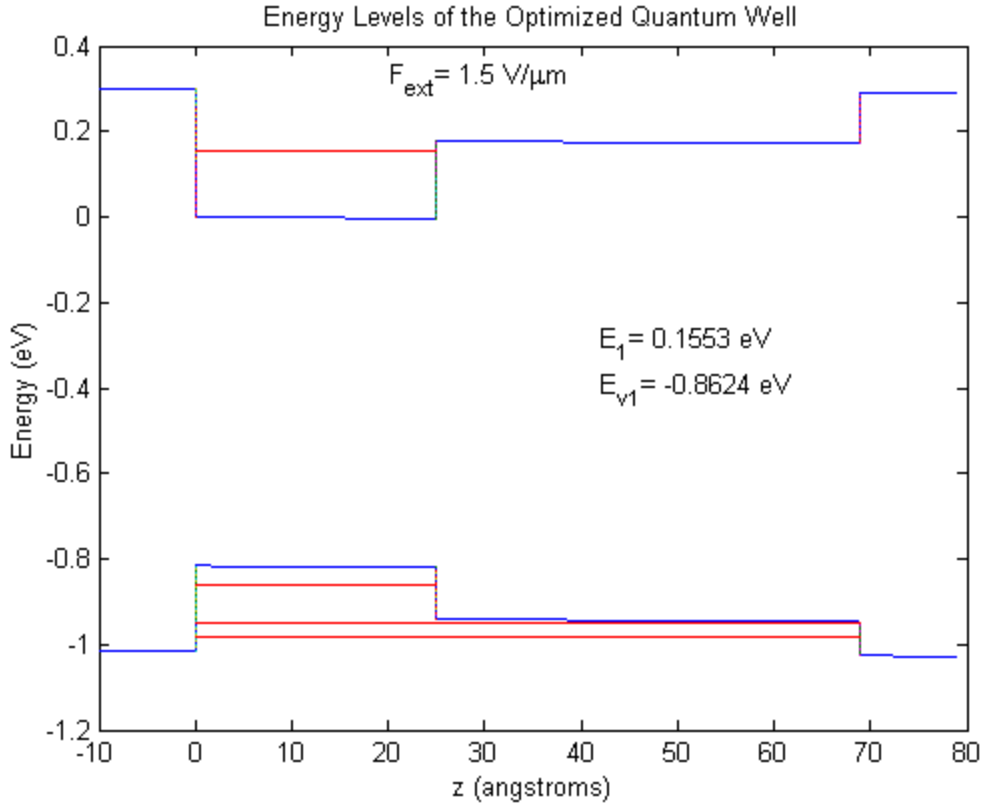
Figure 4.3   Optimized quantum well structure and energy levels with $F_{ext}=1.5V/\mu m$.
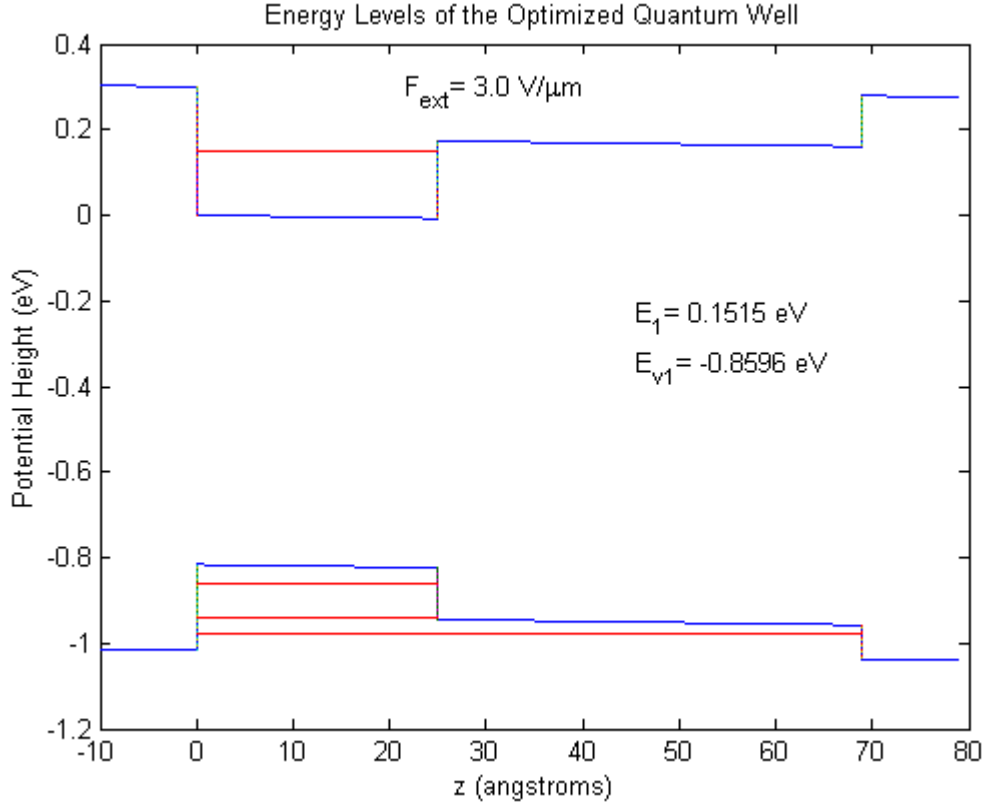
Figure 4.4　　Optimized quantum well structure and energy levels with $F_{ext}=3V/\mu m$.

It is easy to see in these Figures that the second energy level has indeed been pushed up into the continuum where it can easily create a photocurrent.

The main factor to consider in the evaluation of this design is how the application of the external bias will affect the quantum well's ability to detect the designated wavelengths of 1.06 μm and 8-10 μm band. Figure 4.5 shows a comparison between the absorption coefficient for the unbiased well where bound-to-bound absorption occurs and for the case when $F_{ext} = 1.5V/\mu m$ where bound-to-continuum absorption occurs.
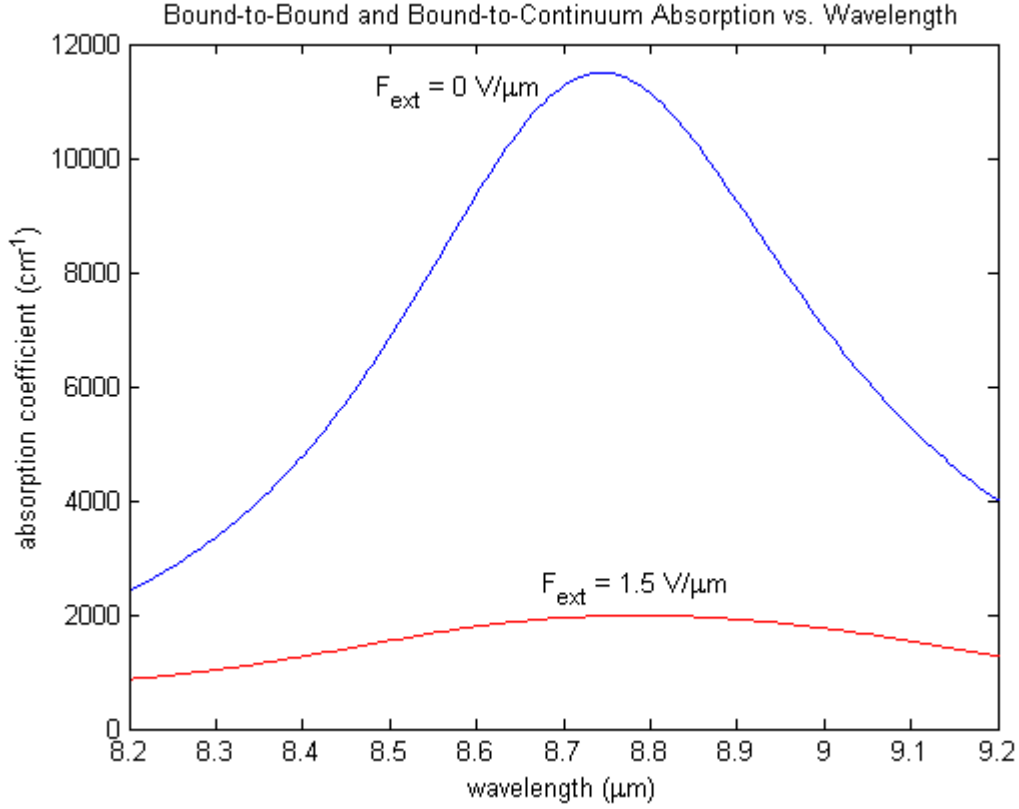
Figure 4.5   Comparison of the absorption coefficients for the unbiased well (bound-to-bound) and the biased well (bound-to-continuum) with $F_{ext} = 1.5 V/\mu m$ and $\Gamma = 10 meV$.

This Figure demonstrates the relative strengths of the bound-to-bound and bound-to-continuum absorption coefficients. The bound-to-bound absorption coefficient has a narrow spectral width compared to the broad bound-to-continuum spectrum as illustrated in Figure 4.6 using the normalized absorption coefficients.
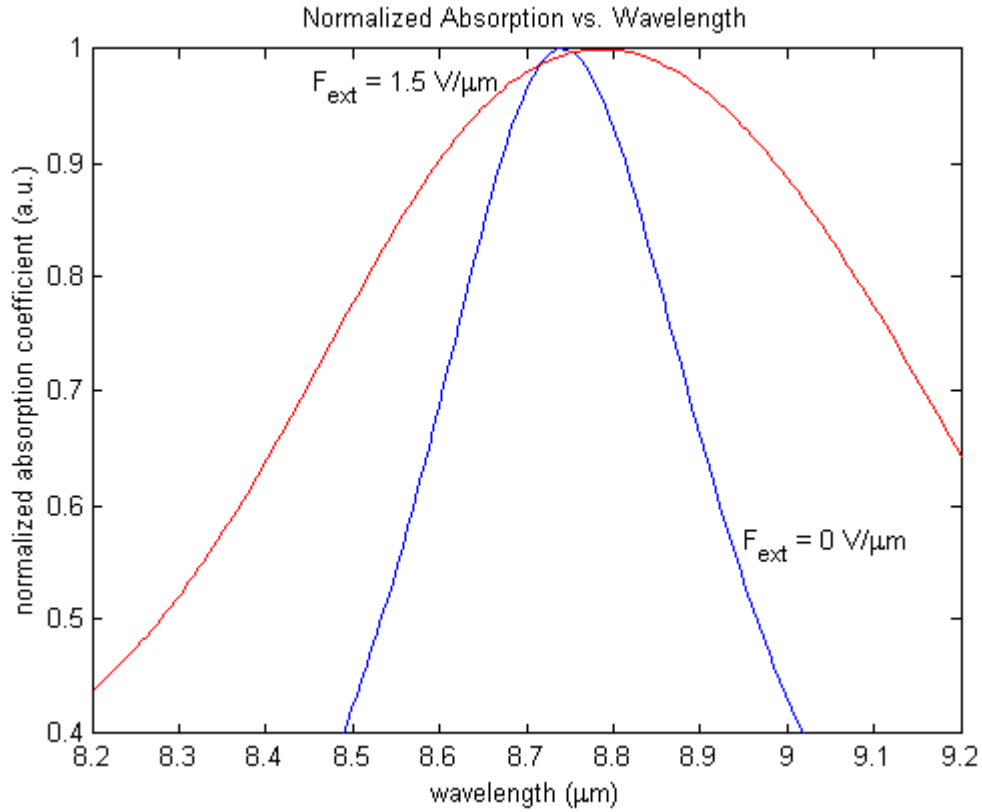
Figure 4.6   Comparison of the normalized absorption coefficients for the unbiased well (bound-to-bound) and the biased well (bound-to-continuum) with $F_{ext}=1.5V/\mu m$ and $\Gamma=10meV$.

Although the shift from bound-to-bound to bound-to-continuum absorption has dropped the relative height of the absorption spectrum it has not dropped to a point where it would be difficult to measure. The broadening of the absorption spectrum has also ensured that the quantum well structure will still be able to detect the MIRW reasonably well and as long as the external bias is not too large, the QWIP should operate as designed. It is important to mention that this thesis has not considered interband absorption due to the difficulties in defining and integrating the Bloch functions in each material, but it can safely be assumed that the interband absorption curve will follow the same pattern that the intersubband absorption curve did and therefore the quantum well structure will also detect the 1.06 µm wavelength reasonably well.

C. SUMMARY

This chapter introduced the optimized design of the quantum well structure used in this thesis along with some of the reasons why the materials used in this quantum well were chosen over other materials. It was also shown that the optimized quantum well structure would operate as a multicolor detector for the specified wavelengths with or without an external bias.

V. CONCLUSION

An asymmetric quantum well device capable of achieving two-color detection through the use of bandgap engineering was demonstrated and the properties of this device were derived and discussed. The ability of the optimized device to detect both short infrared wavelengths and middle infrared wavelengths could be useful as a dual infrared imager/laser spot tracker in military aircraft for the use of accurate ordinance delivery.

The detailed quantum well structure and eigen energy levels of the device were derived through the use of a transfer matrix method with effective mass approximation and the intersubband absorption spectrum for both bound-to-bound and bound-to-continuum transitions was derived and utilized to optimize the device parameters. A transfer matrix method using Airy functions was derived to model the effects of an external bias on the device and the output of this computer model was compared to experimental data and shown to be a good approximation to real life. The reasoning for the choice of the materials used in the optimized design was discussed including a discussion of why other materials that were tried did not work for the chosen wavelengths.

This thesis has shown that an efficient laser spot tracker/infrared imager quantum well device is plausible and further study is warranted. A sample of the optimized design should be grown and tested in order to compare experimental results with the theory presented in this thesis.

THIS PAGE INTENTIONALLY LEFT BLANK

APPENDIX. [PROGRAMMING NOTES AND SELECTED PROGRAMS]

Since many of the calculations presented in this thesis involved a substantial amount of matrix operations the choice of Matlab to create the computer model was manifest. Matlab proved to be an extremely efficient and reliable tool for deriving the energy levels, wavefunctions and absorption spectra for the unbiased quantum well devices. However, the use of Matlab to model the biased quantum well had some limitations due to the Airy functions. Matlab contains the numerical values of the Airy functions, but as expected, these values become unmanageable when the argument in the Airy functions becomes very large or small. An attempt was made to manually insert the asymptotic versions of the Airy functions into the program to overcome this limitation, but this too proved to be unmanageable. Therefore the program written to model the quantum well under an applied field is limited in its scope. The following is a selection of programs used in this thesis to obtain the theoretical data discussed above.

```
%This program is titled aqw_InGaAsP%
%Created: January 2002
%Author: Kevin Lantz


%This is a program to find the energy levels in a two-step quantum well.

%There are three interfaces in this well and therefore will be three transfer matrices to calculate.
%The basic design of the well is as follows:
        %Region 1 (-Inf->0)-->InGaAsP

        %Region 2 (0->a)-->InGaAs
        %Region 3 (a->L)-->InGaAsP
        %Region 4 (L->Inf)-->InGaAsP


clc
global E
% inputs---------------------------------------------------
X1 = input('Percentage of InGaAs (0-1) in region 1       ');
X2 = input('Percentage of In (0-1) in region 2               ');
X3 = input('Percentage of InGaAs (0-1) in region 3       ');

width1 = Inf;   %Extends from -Infinity to 0;
width2 = input('Length of 0->a in angstroms:                 ');
width3 = input('Length of a->L in angstroms:                 ');
width4 = Inf;   %Extends from L to Infinity;


%Energy gap values in each region----------------------------
eg1 = 1.4236*(1-X1) + 0.81612*X1 - 0.13*(X1*(1-X1));
eg2 = 1.519*(1-X2) + 0.417*X2 - 0.477*(X2*(1-X2));
eg3 = 1.4236*(1-X3) + 0.81612*X3 - 0.13*(X3*(1-X3));
eg4 = 1.4236*(1-X1) + 0.81612*X1 - 0.13*(X1*(1-X1));

%Potential Heights in Conduction Band-------------------------
V1 = 0.6*(eg1 - eg2);
V2 = 0;                 %Choose the origin as the bottom left corner of region 2.
V3 = 0.6*(eg3 - eg2);
V4 = V1;


%----------------------------------------------------------------------------
y = 1;     %Initial value of y to correct the logic of the later condition;
a =1;
%constants------------------------------------------------------
hbar = 1.055e-34;   %hbar in ev*m
m0 = 9.11e-31;        %Rest mass of the electron in eV
q = 1.602e-19;

L1 = width1*1e-10;       %Change input of angstroms->meters
L2 = width2*1e-10;
L3 = (width2+width3)*1e-10;
L4 = width4*1e-10;

%Effective electron mass in each region-------------------------
m_eff1 = 1/((X1/(0.0365*m0)) + ((1-X1)/(0.0795*m0)));
m_eff2 = 1/((X2/(0.026*m0)) + ((1-X2)/(0.067*m0)));
m_eff3 = 1/((X3/(0.0365*m0)) + ((1-X3)/(0.0795*m0)));
```

52

```
m_eff4 = 1/((X1/(0.0365*m0)) + ((1-X1)/(0.0795*m0)));

for E = 0.0001:0.0001:(V1-0.0001);

%Determine the values of k---------------------------------------

k1 = sqrt((2*m_eff1*(E - V1)*q)/(hbar^2));
k2 = sqrt((2*m_eff2*(E - V2)*q)/(hbar^2));
k3 = sqrt((2*m_eff3*(E - V3)*q)/(hbar^2));
k4 = sqrt((2*m_eff4*(E - V4)*q)/(hbar^2));

%Determine the transfer matrices---------------------------------

x1 = 0;    %Interface Locations;
x2 = L2;
x3 = L3;

m11 = ((1/2)*((1 + ((k1*m_eff2)/(k2*m_eff1)))*exp(i*(x1*(k1 - k2)))));
m12 = ((1/2)*((1 - ((k1*m_eff2)/(k2*m_eff1)))*exp(-(i*(x1*(k1 + k2))))));
m21 = ((1/2)*((1 - ((k1*m_eff2)/(k2*m_eff1)))*exp(i*(x1*(k1 + k2)))));
m22 = ((1/2)*((1 + ((k1*m_eff2)/(k2*m_eff1)))*exp(-(i*(x1*(k1 - k2))))));

m_11 = ((1/2)*((1 + ((k2*m_eff3)/(k3*m_eff2)))*exp(i*(x2*(k2 - k3)))));
m_12 = ((1/2)*((1 - ((k2*m_eff3)/(k3*m_eff2)))*exp(-(i*(x2*(k2 + k3))))));
m_21 = ((1/2)*((1 - ((k2*m_eff3)/(k3*m_eff2)))*exp(i*(x2*(k2 + k3)))));
m_22 = ((1/2)*((1 + ((k2*m_eff3)/(k3*m_eff2)))*exp(-(i*(x2*(k2 - k3))))));

m_11_ = ((1/2)*((1 + ((k3*m_eff4)/(k4*m_eff3)))*exp(i*(x3*(k3 - k4)))));
m_12_ = ((1/2)*((1 - ((k3*m_eff4)/(k4*m_eff3)))*exp(-(i*(x3*(k3 + k4))))));
m_21_ = ((1/2)*((1 - ((k3*m_eff4)/(k4*m_eff3)))*exp(i*(x3*(k3 + k4)))));
m_22_ = ((1/2)*((1 + ((k3*m_eff4)/(k4*m_eff3)))*exp(-(i*(x3*(k3 - k4))))));

M1 = [m11,m12;m21,m22];
M2 = [m_11,m_12;m_21,m_22];
M3 = [m_11_,m_12_;m_21_,m_22_];

%Now we find an expression for M22------------------------------------

B = M3*M2*M1;
J22 = B(2,2);

%Program used to calculate and plot the wavefunctions------------------

Psi_aqw

%Define the function y-------------------------------------------

z = y;
y = real(J22);

%Define condition for energy eigenvalues-------------------------------

if z.*y < 0

   disp(E)
   Eout(a) = E;    %Stores energy levels into an array
```

```
    a = a+1;

    %plotting the wavefunctions----------------------------
    hold on
    plot((X*1e10),((psi1/20)+E))
    plot((Y*1e10),((psi2/20)+E))
    plot((Z*1e10),((psi3/20)+E))
    plot((T*1e10),((psi4/20)+E))

end

end

%This program finds the energy levels in the Valence Band

valence_InGaAsP

%Drawing the finite well-----------------------------------------

well2   %This program draws the Conduction band well


%---------------------End of aqw_InGaAsP-----------------------------
```

```
%This program is titled Psi_aqw
%Created: January 2002
%Author: Kevin Lantz


%This is a program that is used to find the wavefunctions in each region of the quantum well.
%The bulk of this program is trying to find the normalization constant b1, which determines the
%normalized wavefunctions and the coefficients A1,B1,A2,B2,A3,B3,A4,B4...

deltax = 1e-10;

%All of the coefficients can be written in terms of B1

B1 = 1; %dummy variable...actual B1 is B1*b1 == b1
A2 = m12*B1;
B2 = m22*B1;
A3 = (m_11*m12 + m_12*m22)*B1;
B3 = (m_21*m12 + m_22*m22)*B1;
A4 = (m_11_*(m_11*m12 + m_12*m22) + m_12_*(m_21*m12 + m_22*m22))*B1;

%Defining the regions of the quantum well-------------
X = -(50*deltax):deltax:0;
Y = 0:deltax:L2;
Z = L2:deltax:L3;
T = L3:deltax:L3+(50*deltax);

%Defining the unnormalized wavefunctions--------------
psi1 = B1*exp(-(i*k1*X));
psi2 = A2*exp(i*k2*Y) + B2*exp(-(i*k2*Y));
psi3 = A3*exp(i*k3*Z) + B3*exp(-(i*k3*Z));
psi4 = A4*exp(i*k4*T);

%Integrating----------------------------------------------
psi_1 = conj(psi1);
psi_2 = conj(psi2);
psi_3 = conj(psi3);
psi_4 = conj(psi4);
% the integral over all space of |psi|^2 == psi*conj(psi) has to be 1

integrand1 = (psi1.*psi_1)*deltax;
integrand2 = (psi2.*psi_2)*deltax;
integrand3 = (psi3.*psi_3)*deltax;
integrand4 = (psi4.*psi_4)*deltax;

integral1 = sum(integrand1);
integral2 = sum(integrand2);
integral3 = sum(integrand3);
integral4 = sum(integrand4);

finali = integral1 + integral2 + integral3 + integral4;

b1 = 1/(sqrt(finali));      %normalization constant
```

% normalized wavefunctions are just the unnormalized wavefunctions multiplied by the normalization constant

```
Psi1 = b1*psi1;
Psi2 = b1*psi2;
Psi3 = b1*psi3;
Psi4 = b1*psi4;

% This part of the program integrates the normalized wavefunction in order to check
%that it equals 1.
%This is used to make sure that the program is working...

Psi_1 = conj(Psi1);
Psi_2 = conj(Psi2);
Psi_3 = conj(Psi3);
Psi_4 = conj(Psi4);

Integrand1 = (Psi1.*Psi_1)*deltax;
Integrand2 = (Psi2.*Psi_2)*deltax;
Integrand3 = (Psi3.*Psi_3)*deltax;
Integrand4 = (Psi4.*Psi_4)*deltax;

Integral1 = sum(Integrand1);
Integral2 = sum(Integrand2);
Integral3 = sum(Integrand3);
Integral4 = sum(Integrand4);

finalI = Integral1 + Integral2 + Integral3 + Integral4;

%---------------------------------End of Psi_aqw-----------------------------------------
```

```
%This program is titled E_InGaAsP
%Created: February 2002
%Author: Kevin Lantz

%This program has the same form as aqw_InGaAsP except it uses Airy functions

clc
F = input('Electric Field in [V/m]:        ');

X1_ = input('Percentage of Al (0-1) in region 1:      ');
X2_ = input('Percentage of Al (0-1) in region 2:      ');
X3_ = input('Percentage of Al (0-1) in region 3:      ');
X4_ = X1_;

width1 = Inf;   %Extends from -Infinity to 0;
width2 = input('Width of the region 0->a in angstroms:    ');  %Well width
width3 = input('Width of the region a->b in angstroms:    ');
width4 = Inf;   %Extends from L to Infinity;
%----------------------------------------------------------------------------------------------
y = 0;      %Initial value of y to correct the logic of the later condition
a = 1;
%--------------------------------%

L1 = width1*1e-10;      %Change input of angstroms->meters
L2 = width2*1e-10;
L3 = (width2+width3)*1e-10;
L4 = width4*1e-10;

hbar = 1.055e-34;  %[J*s]
m0 = 9.11e-31; %[kg]
e = 1.602e-19; %[C]

%Conditions used to make the program function correctly under positive or negative bias
if F < 0;
    z1 = L3;
    z2 = L2;
    z3 = 0;
    X1 = X4_;
    X2 = X3_;
    X3 = X2_;
    X4 = X1_;
else
    z1 = 0;
    z2 = L2;
    z3 = L3;
    X1 = X1_;
    X2 = X2_;
    X3 = X3_;
    X4 = X4_;
end
%----------------------------------%

if F < 0
    eg1 = 1.4236*(1-X1) + 0.81612*X1 - 0.13*(X1*(1-X1));
    eg3 = 1.519*(1-X2) + 0.417*X2 - 0.477*(X2*(1-X2));
    eg2 = 1.4236*(1-X3) + 0.81612*X3 - 0.13*(X3*(1-X3));
```

```
      eg4 = 1.4236*(1-X1) + 0.81612*X1 - 0.13*(X1*(1-X1));
      m_eff1 = 1/((X1/(0.0365*m0)) + ((1-X1)/(0.0795*m0)));
      m_eff3 = 1/((X2/(0.026*m0)) + ((1-X2)/(0.067*m0)));
      m_eff2 = 1/((X3/(0.0365*m0)) + ((1-X3)/(0.0795*m0)));
      m_eff4 = 1/((X1/(0.0365*m0)) + ((1-X1)/(0.0795*m0)));

  else
      eg1 = 1.4236*(1-X1) + 0.81612*X1 - 0.13*(X1*(1-X1));
      eg2 = 1.519*(1-X2) + 0.417*X2 - 0.477*(X2*(1-X2));
      eg3 = 1.4236*(1-X3) + 0.81612*X3 - 0.13*(X3*(1-X3));
      eg4 = 1.4236*(1-X1) + 0.81612*X1 - 0.13*(X1*(1-X1));
      m_eff1 = 1/((X1/(0.0365*m0)) + ((1-X1)/(0.0795*m0)));
      m_eff2 = 1/((X2/(0.026*m0)) + ((1-X2)/(0.067*m0)));
      m_eff3 = 1/((X3/(0.0365*m0)) + ((1-X3)/(0.0795*m0)));
      m_eff4 = 1/((X1/(0.0365*m0)) + ((1-X1)/(0.0795*m0)));
  end


V1 = 0.6*(eg1 - 0.8161193);
V2 = 0.6*(eg2 - 0.8161193);   %Choose the origin as the bottom left corner of region 2.
V3 = 0.6*(eg3 - 0.8161193);
V4 = V1;
%--------------------------------%
C1 = (((2*m_eff1*e)/((F*hbar)^2))^(1/3));
C2 = (((2*m_eff2*e)/((F*hbar)^2))^(1/3));
C3 = (((2*m_eff3*e)/((F*hbar)^2))^(1/3));
C4 = (((2*m_eff4*e)/((F*hbar)^2))^(1/3));

sigma1 = ((m_eff1*C2)/(m_eff2*C1));
sigma2 = ((m_eff2*C3)/(m_eff3*C2));
sigma3 = ((m_eff3*C4)/(m_eff4*C3));


%---------------------------------%
if F < 0;
   DD = 0;
   V2_ = V1;
else
   DD = -F*L2;
   V2_ = V1 - F*L3;
end
%---------------------------------%
for E =DD:0.001:V2_;

eta1 = (E - V1);
eta2 = (E - V2);
eta3 = (E - V3);
eta4 = (E - V4);


Alpha1 = -C1*(F*z1 + eta1);
Alpha2 = -C2*(F*z1 + eta2);
Alpha2_ = -C2*(F*z2 + eta2);
Alpha3 = -C3*(F*z2 + eta3);
Alpha3_ = -C3*(F*z3 + eta3);
Alpha4 = -C4*(F*z3 + eta4);

%-------------------------------------%
```

```
m11 = (pi)*(airy(Alpha2)*airy(3,Alpha1) - sigma1*(airy(2,Alpha1)*airy(1,Alpha2)));
m12 = (pi)*(airy(2,Alpha2)*airy(3,Alpha1) - sigma1*(airy(2,Alpha1)*airy(3,Alpha2)));
m21 = (pi)*(sigma1*(airy(Alpha1)*airy(1,Alpha2)) - airy(1,Alpha1)*airy(Alpha2));
m22 = (pi)*(sigma1*(airy(Alpha1)*airy(3,Alpha2)) - airy(1,Alpha1)*airy(2,Alpha2));

m_11 = (pi)*(airy(Alpha3)*airy(3,Alpha2_) - sigma2*(airy(2,Alpha2_)*airy(1,Alpha3)));
m_12 = (pi)*(airy(2,Alpha3)*airy(3,Alpha2_) - sigma2*(airy(2,Alpha2_)*airy(3,Alpha3)));
m_21 = (pi)*(sigma2*(airy(Alpha2_)*airy(1,Alpha3)) - airy(1,Alpha2_)*airy(Alpha3));
m_22 = (pi)*(sigma2*(airy(Alpha2_)*airy(3,Alpha3)) - airy(1,Alpha2_)*airy(2,Alpha3));

m_11_ = (pi)*(airy(Alpha4)*airy(3,Alpha3_) - sigma3*(airy(2,Alpha3_)*airy(1,Alpha4)));
m_12_ = (pi)*(airy(2,Alpha4)*airy(3,Alpha3_) - sigma3*(airy(2,Alpha3_)*airy(3,Alpha4)));
m_21_ = (pi)*(sigma3*(airy(Alpha3_)*airy(1,Alpha4)) - airy(1,Alpha3_)*airy(Alpha4));
m_22_ = (pi)*(sigma3*(airy(Alpha3_)*airy(3,Alpha4)) - airy(1,Alpha3_)*airy(2,Alpha4));

M1 = [m11,m12;m21,m22];
M2 = [m_11,m_12;m_21,m_22];
M3 = [m_11_,m_12_;m_21_,m_22_];

M2M3 = M2*M3;
M = M1*M2*M3;

M22 = real(M(2,2));

Epsi_aqw

z = y;
y = M22;

if z.*y < 0
    disp(E)
    Eout(a) = E;
    a = a + 1;
    hold on

    plot((X*1e10),((Psi1./(4e5))+E))
    plot((Y*1e10),((Psi2./(4e5))+E))
    plot((Z*1e10),((Psi3./(4e5))+E))
    plot((T*1e10),((Psi4./(4e5))+E))


end

end
E_valence_InGaAsP

Ewell2

%--------------------End of E_InGaAsP--------------------------
```

```matlab
%This program is titled absorption.
%Created: February 2002
%Author: Kevin Lantz
%This program uses the wavefunctions to find the bound-to-bound and bound-to-continuum
%absorption spectra.

clc
aqw_InGaAsP


%--------------Psi at Eout(1)------------

kE1_1 = sqrt((2*m_eff1*(Eout(1)-V1)*q)/(hbar^2));
kE1_2 = sqrt((2*m_eff2*(Eout(1)-V2)*q)/(hbar^2));
kE1_3 = sqrt((2*m_eff3*(Eout(1)-V3)*q)/(hbar^2));
kE1_4 = sqrt((2*m_eff4*(Eout(1)-V4)*q)/(hbar^2));


mE1_11 = ((1/2)*((1 + ((kE1_1*m_eff2)/(kE1_2*m_eff1)))*exp(i*(x1*(kE1_1 - kE1_2)))));
mE1_12 = ((1/2)*((1 - ((kE1_1*m_eff2)/(kE1_2*m_eff1)))*exp(-(i*(x1*(kE1_1 + kE1_2))))));
mE1_21 = ((1/2)*((1 - ((kE1_1*m_eff2)/(kE1_2*m_eff1)))*exp(i*(x1*(kE1_1 + kE1_2)))));
mE1_22 = ((1/2)*((1 + ((kE1_1*m_eff2)/(kE1_2*m_eff1)))*exp(-(i*(x1*(kE1_1 - kE1_2))))));


m_E1_11 = ((1/2)*((1 + ((kE1_2*m_eff3)/(kE1_3*m_eff2)))*exp(i*(x2*(kE1_2 - kE1_3)))));
m_E1_12 = ((1/2)*((1 - ((kE1_2*m_eff3)/(kE1_3*m_eff2)))*exp(-(i*(x2*(kE1_2 + kE1_3))))));
m_E1_21 = ((1/2)*((1 - ((kE1_2*m_eff3)/(kE1_3*m_eff2)))*exp(i*(x2*(kE1_2 + kE1_3)))));
m_E1_22 = ((1/2)*((1 + ((kE1_2*m_eff3)/(kE1_3*m_eff2)))*exp(-(i*(x2*(kE1_2 - kE1_3))))));


m_E1_11_ = ((1/2)*((1 + ((kE1_3*m_eff4)/(kE1_4*m_eff3)))*exp(i*(x3*(kE1_3 - kE1_4)))));
m_E1_12_ = ((1/2)*((1 - ((kE1_3*m_eff4)/(kE1_4*m_eff3)))*exp(-(i*(x3*(kE1_3 + kE1_4))))));
m_E1_21_ = ((1/2)*((1 - ((kE1_3*m_eff4)/(kE1_4*m_eff3)))*exp(i*(x3*(kE1_3 + kE1_4)))));
m_E1_22_ = ((1/2)*((1 + ((kE1_3*m_eff4)/(kE1_4*m_eff3)))*exp(-(i*(x3*(kE1_3 - kE1_4))))));

ME1_1 = [mE1_11,mE1_12;mE1_21,mE1_22];
ME1_2 = [m_E1_11,m_E1_12;m_E1_21,m_E1_22];
ME1_3 = [m_E1_11_,m_E1_12_;m_E1_21_,m_E1_22_];

M2M1 = ME1_2*ME1_1;
M3M2M1 = ME1_3*ME1_2*ME1_1;

AE1_1 = 0;
BE1_1 = 1;
AE1_2 = ME1_1(1,1)*AE1_1 + ME1_1(1,2)*BE1_1;
BE1_2 = ME1_1(2,1)*AE1_1 + ME1_1(2,2)*BE1_1;
AE1_3 = M2M1(1,1)*AE1_1 + M2M1(1,2)*BE1_1;
BE1_3 = M2M1(2,1)*AE1_1 + M2M1(2,2)*BE1_1;
AE1_4 = M3M2M1(1,1)*AE1_1 + M3M2M1(1,2)*BE1_1;
BE1_4 = 0;

deltax = 1e-10;

X = -L3:deltax:0;
Y = 0:deltax:L2;
Z = L2:deltax:L3;
T = L3:deltax:(2*L3);

psiE1_1 = AE1_1*exp(i*kE1_1*X) + BE1_1*exp(-(i*kE1_1*X));
```

```
psiE1_2 = AE1_2*exp(i*kE1_2*Y) + BE1_2*exp(-(i*kE1_2*Y));
psiE1_3 = AE1_3*exp(i*kE1_3*Z) + BE1_3*exp(-(i*kE1_3*Z));
psiE1_4 = AE1_4*exp(i*kE1_4*T) + BE1_4*exp(-(i*kE1_4*T));

psi_E1_1 = conj(psiE1_1);
psi_E1_2 = conj(psiE1_2);
psi_E1_3 = conj(psiE1_3);
psi_E1_4 = conj(psiE1_4);

deltaIE1_1 = (psi_E1_1.*psiE1_1)*deltax;
deltaIE1_2 = (psi_E1_2.*psiE1_2)*deltax;
deltaIE1_3 = (psi_E1_3.*psiE1_3)*deltax;
deltaIE1_4 = (psi_E1_4.*psiE1_4)*deltax;

IE1_1 = sum(deltaIE1_1);
IE1_2 = sum(deltaIE1_2);
IE1_3 = sum(deltaIE1_3);
IE1_4 = sum(deltaIE1_4);

finalE1 = IE1_1+IE1_2+IE1_3+IE1_4;

bE1 = 1/(sqrt(finalE1));

PsiE1_1 = bE1*psiE1_1;
PsiE1_2 = bE1*psiE1_2;
PsiE1_3 = bE1*psiE1_3;
PsiE1_4 = bE1*psiE1_4;

%----------------derivative of Psi at Eout(1)-------------

psiEE1_1 = AE1_1*exp(i*kE1_1*X) - BE1_1*exp(-(i*kE1_1*X));
psiEE1_2 = AE1_2*exp(i*kE1_2*Y) - BE1_2*exp(-(i*kE1_2*Y));
psiEE1_3 = AE1_3*exp(i*kE1_3*Z) - BE1_3*exp(-(i*kE1_3*Z));
psiEE1_4 = AE1_4*exp(i*kE1_4*T) - BE1_4*exp(-(i*kE1_4*T));

PsiEE1_1 = bE1*psiEE1_1;
PsiEE1_2 = bE1*psiEE1_2;
PsiEE1_3 = bE1*psiEE1_3;
PsiEE1_4 = bE1*psiEE1_4;

%-----------------Psi at Eout(2)--------------------------

kE2_1 = sqrt((2*m_eff1*(Eout(2)-V1)*q)/(hbar^2));
kE2_2 = sqrt((2*m_eff2*(Eout(2)-V2)*q)/(hbar^2));
kE2_3 = sqrt((2*m_eff3*(Eout(2)-V3)*q)/(hbar^2));
kE2_4 = sqrt((2*m_eff4*(Eout(2)-V4)*q)/(hbar^2));

mE2_11 = ((1/2)*((1 + ((kE2_1*m_eff2)/(kE2_2*m_eff1)))*exp(i*(x1*(kE2_1 - kE2_2)))));
mE2_12 = ((1/2)*((1 - ((kE2_1*m_eff2)/(kE2_2*m_eff1)))*exp(-(i*(x1*(kE2_1 + kE2_2))))));
mE2_21 = ((1/2)*((1 - ((kE2_1*m_eff2)/(kE2_2*m_eff1)))*exp(i*(x1*(kE2_1 + kE2_2)))));
mE2_22 = ((1/2)*((1 + ((kE2_1*m_eff2)/(kE2_2*m_eff1)))*exp(-(i*(x1*(kE2_1 - kE2_2))))));

m_E2_11 = ((1/2)*((1 + ((kE2_2*m_eff3)/(kE2_3*m_eff2)))*exp(i*(x2*(kE2_2 - kE2_3)))));
m_E2_12 = ((1/2)*((1 - ((kE2_2*m_eff3)/(kE2_3*m_eff2)))*exp(-(i*(x2*(kE2_2 + kE2_3))))));
m_E2_21 = ((1/2)*((1 - ((kE2_2*m_eff3)/(kE2_3*m_eff2)))*exp(i*(x2*(kE2_2 + kE2_3)))));
m_E2_22 = ((1/2)*((1 + ((kE2_2*m_eff3)/(kE2_3*m_eff2)))*exp(-(i*(x2*(kE2_2 - kE2_3))))));
```

61

```
m_E2_11_ = ((1/2)*((1 + ((kE2_3*m_eff4)/(kE2_4*m_eff3)))*exp(i*(x3*(kE2_3 - kE2_4)))));
m_E2_12_ = ((1/2)*((1 - ((kE2_3*m_eff4)/(kE2_4*m_eff3)))*exp(-(i*(x3*(kE2_3 + kE2_4))))));
m_E2_21_ = ((1/2)*((1 - ((kE2_3*m_eff4)/(kE2_4*m_eff3)))*exp(i*(x3*(kE2_3 + kE2_4)))));
m_E2_22_ = ((1/2)*((1 + ((kE2_3*m_eff4)/(kE2_4*m_eff3)))*exp(-(i*(x3*(kE2_3 - kE2_4))))));

ME2_1 = [mE2_11,mE2_12;mE2_21,mE2_22];
ME2_2 = [m_E2_11,m_E2_12;m_E2_21,m_E2_22];
ME2_3 = [m_E2_11_,m_E2_12_;m_E2_21_,m_E2_22_];

M2_M1 = ME2_2*ME2_1;
M3M2_M1 = ME2_3*ME2_2*ME2_1;

AE2_1 = 0;
BE2_1 = 1;
AE2_2 = ME2_1(1,1)*AE2_1 + ME2_1(1,2)*BE2_1;
BE2_2 = ME2_1(2,1)*AE2_1 + ME2_1(2,2)*BE2_1;
AE2_3 = M2_M1(1,1)*AE2_1 + M2_M1(1,2)*BE2_1;
BE2_3 = M2_M1(2,1)*AE2_1 + M2_M1(2,2)*BE2_1;
AE2_4 = M3M2_M1(1,1)*AE2_1 + M3M2_M1(1,2)*BE2_1;
BE2_4 = 0;

psiE2_1 = AE2_1*exp(i*kE2_1*X) + BE2_1*exp(-(i*kE2_1*X));
psiE2_2 = AE2_2*exp(i*kE2_2*Y) + BE2_2*exp(-(i*kE2_2*Y));
psiE2_3 = AE2_3*exp(i*kE2_3*Z) + BE2_3*exp(-(i*kE2_3*Z));
psiE2_4 = AE2_4*exp(i*kE2_4*T) + BE2_4*exp(-(i*kE2_4*T));

psi_E2_1 = conj(psiE2_1);
psi_E2_2 = conj(psiE2_2);
psi_E2_3 = conj(psiE2_3);
psi_E2_4 = conj(psiE2_4);

deltaIE2_1 = (psi_E2_1.*psiE2_1)*deltax;
deltaIE2_2 = (psi_E2_2.*psiE2_2)*deltax;
deltaIE2_3 = (psi_E2_3.*psiE2_3)*deltax;
deltaIE2_4 = (psi_E2_4.*psiE2_4)*deltax;

IE2_1 = sum(deltaIE2_1);
IE2_2 = sum(deltaIE2_2);
IE2_3 = sum(deltaIE2_3);
IE2_4 = sum(deltaIE2_4);

finalE2 = IE2_1+IE2_2+IE2_3+IE2_4;

bE2 = 1/(sqrt(finalE2));

PsiE2_1 = bE2*psiE2_1;
PsiE2_2 = bE2*psiE2_2;
PsiE2_3 = bE2*psiE2_3;
PsiE2_4 = bE2*psiE2_4;

PsiE2_1_ = conj(PsiE2_1);
PsiE2_2_ = conj(PsiE2_2);
PsiE2_3_ = conj(PsiE2_3);
PsiE2_4_ = conj(PsiE2_4);
```

```
%-----------------<Psi(Eout(2))*|k|Psi(Eout(1))>----------

deltaE12_1 = (PsiE2_1_.*kE1_1.*PsiEE1_1)*deltax;
deltaE12_2 = (PsiE2_2_.*kE1_2.*PsiEE1_2)*deltax;
deltaE12_3 = (PsiE2_3_.*kE1_3.*PsiEE1_3)*deltax;
deltaE12_4 = (PsiE2_4_.*kE1_4.*PsiEE1_4)*deltax;

E12_1 = sum(deltaE12_1);
E12_2 = sum(deltaE12_2);
E12_3 = sum(deltaE12_3);
E12_4 = sum(deltaE12_4);

averageE12 = E12_1+E12_2+E12_3+E12_4;

AverageE12 = averageE12*(conj(averageE12));

%------------------Line Shape----------------------------
N = 1e24;
e0 = 8.85e-12;
c = 3e8;
n = 3.5;
Gamma = ((10e-3)*q)/2;
ap = 1;

for EE = (Eout(1)-0.1):1e-4:(V1-0.001);

g = (Gamma)/((((Eout(2)-Eout(1)-EE)*q)^2)+((Gamma)^2));
gmax = (Gamma)/(((((0)*q)^2)+((Gamma)^2));
C = (N*(q^2)*(hbar^3))/((m_eff1^2)*e0*n*c);
alphaE12(ap) = (C.*g.*AverageE12)/(EE*q);

ap = ap + 1;
end

%
%---------------Psi above the well------------------------;
r=1;
for Energy = (V1+0.0001):0.0001:(V1+.025)


kA1 = sqrt((2*m_eff1*(Energy-V1)*q)/(hbar^2));
kA2 = sqrt((2*m_eff2*(Energy-V2)*q)/(hbar^2));
kA3 = sqrt((2*m_eff3*(Energy-V3)*q)/(hbar^2));
kA4 = sqrt((2*m_eff4*(Energy-V4)*q)/(hbar^2));

mA_11 = ((1/2)*((1 + ((kA1*m_eff2)/(kA2*m_eff1)))*exp(i*(x1*(kA1 - kA2)))));
mA_12 = ((1/2)*((1 - ((kA1*m_eff2)/(kA2*m_eff1)))*exp(-(i*(x1*(kA1 + kA2))))));
mA_21 = ((1/2)*((1 - ((kA1*m_eff2)/(kA2*m_eff1)))*exp(i*(x1*(kA1 + kA2)))));
mA_22 = ((1/2)*((1 + ((kA1*m_eff2)/(kA2*m_eff1)))*exp(-(i*(x1*(kA1 - kA2))))));

m_A_11 = ((1/2)*((1 + ((kA2*m_eff3)/(kA3*m_eff2)))*exp(i*(x2*(kA2 - kA3)))));
m_A_12 = ((1/2)*((1 - ((kA2*m_eff3)/(kA3*m_eff2)))*exp(-(i*(x2*(kA2 + kA3))))));
m_A_21 = ((1/2)*((1 - ((kA2*m_eff3)/(kA3*m_eff2)))*exp(i*(x2*(kA2 + kA3)))));
m_A_22 = ((1/2)*((1 + ((kA2*m_eff3)/(kA3*m_eff2)))*exp(-(i*(x2*(kA2 - kA3))))));

m_A_11_ = ((1/2)*((1 + ((kA3*m_eff4)/(kA4*m_eff3)))*exp(i*(x3*(kA3 - kA4)))));
```

```
m_A_12_ = ((1/2)*((1 - ((kA3*m_eff4)/(kA4*m_eff3)))*exp(-(i*(x3*(kA3 + kA4))))));
m_A_21_ = ((1/2)*((1 - ((kA3*m_eff4)/(kA4*m_eff3)))*exp(i*(x3*(kA3 + kA4)))));
m_A_22_ = ((1/2)*((1 + ((kA3*m_eff4)/(kA4*m_eff3)))*exp(-(i*(x3*(kA3 - kA4))))));

MA_1 = [mA_11,mA_12;mA_21,mA_22];
MA_2 = [m_A_11,m_A_12;m_A_21,m_A_22];
MA_3 = [m_A_11_,m_A_12_;m_A_21_,m_A_22_];

M2M1_ = MA_2*MA_1;
M3M2M1_ = MA_3*MA_2*MA_1;

A1 = 1;
B1 = ((-M3M2M1_(2,1))/(M3M2M1_(2,2)))*A1;
A2 = MA_1(1,1)*A1 + MA_1(1,2)*B1;
B2 = MA_1(2,1)*A1 + MA_1(2,2)*B1;
A3 = M2M1_(1,1)*A1 + M2M1_(1,2)*B1;
B3 = M2M1_(2,1)*A1 + M2M1_(2,2)*B1;
A4 = M3M2M1_(1,1)*A1 + M3M2M1_(1,2)*B1;
B4 = 0;

PsiA1 = A1*exp(i*kA1*X) + B1*exp(-(i*kA1*X));
PsiA2 = A2*exp(i*kA2*Y) + B2*exp(-(i*kA2*Y));
PsiA3 = A3*exp(i*kA3*Z) + B3*exp(-(i*kA3*Z));
PsiA4 = A4*exp(i*kA4*T) + B4*exp(-(i*kA4*T));

PsiA1_ = conj(PsiA1);
PsiA2_ = conj(PsiA2);
PsiA3_ = conj(PsiA3);
PsiA4_ = conj(PsiA4);

%------------------<Psi(above well)*|k|Psi(Eout(1))>------------------


deltaEA_1 = (PsiA1_.*kE1_1.*PsiEE1_1)*deltax;
deltaEA_2 = (PsiA2_.*kE1_2.*PsiEE1_2)*deltax;
deltaEA_3 = (PsiA3_.*kE1_3.*PsiEE1_3)*deltax;
deltaEA_4 = (PsiA4_.*kE1_4.*PsiEE1_4)*deltax;

EA_1 = sum(deltaEA_1);
EA_2 = sum(deltaEA_2);
EA_3 = sum(deltaEA_3);
EA_4 = sum(deltaEA_4);

averageEA = EA_1+EA_2+EA_3+EA_4;

AverageEA(r) = averageEA*(conj(averageEA));

%-------------------Finding the absorption coefficient-------------------

C = (N*(q^2)*(hbar^2))/(2*(m_eff1^2)*e0*n*c);

CC = (((((Energy-V1))*q)^2) + (Gamma^2));

rho = ((1/CC)^(1/4));

C_ = (((Energy-Eout(1))*q)^2);
```

```
A_ = (sqrt((2*m_eff1)/C_))*rho;

alpha(r) = C*A_*AverageEA(r);

r = r + 1;
end

%-----------------End of absorption--------------------------------
```

THIS PAGE INTENTIONALLY LEFT BLANK

LIST OF REFERENCES

Berger, V., N. Vodjdani, P. Bois, B. Vinter and S. Delaitre, "Switchable bicolor infrared detector using an electron transfer infrared modulator", *Appl. Phys. Lett.*, **61**, pp. 1898-1900, 1992.

Chiang, J.C., S.S. Li, M.Z. Tidrow, P. Ho, M. Tsai and C.P. Lee, "A voltage-tunable multicolor triple-coupled InGaAs/GaAs/AlGaAs quantum-well infrared photodetector for 8-12 μm detection", *Appl. Phys. Lett.*, **69**, pp. 2412-2414, 1996.

Choi, K.K. *The Physics of Quantum Well Infrared Photodetectors*, pp. 131-133, World Scientific, 1997

Coon, D.D. and R.P.G. Karunasiri, "New mode of IR detection using quantum wells", *Appl. Phys. Lett.*, **45**, pp.649-651, 1984.

Esaki, L. and R. Tsu, *IBM Research Note*, RC-2418, 1969.

Flatté, M.E., P.M. Young, L.-H. Peng and H. Ehrenreich, "Generalized superlattice $K \cdot p$ theory and intersubband optical transitions", *Phys. Rev. B*, **53**, pp. 1963-1978, 1996.

Hasnain, G., B.F. Levine, D.L. Sivco and A.Y. Cho, "Mid-infrared detectors in the 3-5 μm band using bound to continuum state absorption in InGaAs/InAlAs multiquantum well structures", *Appl. Phys. Lett.*, **56**, pp. 770-772, 1989.

Hewish, Mark and Joris Janssen Lok, "Advance of the pods: enhancing precision attacks night and day", *International Defense Review*, 01 March 2002.

Gravé, I., A. Shakouri, N. Kruze and A. Yariv, "Voltage-controlled tunable GaAs/AlGaAs multistack quantum well infrared detector", *Appl. Phys. Lett.*, **60**, pp. 2362-2364, 1992.

Gunapala, S.D., J.K. Liu, M. Sundaram, S.V. Bandara, C.A. Shott, T. Hoelter, P.D. Maker and R.E. Muller, "Long Wavelength Quantum Well Infrared Photodetector (QWIP) Research at Jet Propulsion Laboratory", *Proc. SPIE*, **2744**, pp. 722-730, 1996.

Kane, E.O., *Jour. Phys. Chem. Sol.*, **1**, pp. 249, 1957.

Karunasiri, R.P.G., Y.J. Mii and K.L. Wang, "Tunable infrared modulator and switch using Stark shift in step quantum wells", *IEEE Electron. Dev. Lett.*, **11**, pp. 227-229, 1990.

Karunasiri, R.P.G., J.S. Park, J. Chen, R. Shih, J.F. Scheihing and M.A. Dodd, "Normal incident InGaAs/GaAs multiple quantum well infrared detector using intersubband transitions", *Appl. Phys. Lett.*, **67**, pp. 2600-2602, 1995.

Köck, A., E. Gornik, G. Abstreiter, G. Böhm, M. Walther and G. Weimann, "Double wavelength selective GaAs/AlGaAs infrared detector device", *Appl. Phys. Lett.*, **60**, pp. 2011-2013, 1992.

Levine, B.F. K.K. Choi, C.G. Bethea, J. Walker and R.J. Malik, "New 10 μm infrared detector using intersubband absorption in resonant tunneling GaAlAs superlattices", *Appl. Phys. Lett.*, **50**, pp. 1092-1094, 1987.

Levine, B.F., A. Zussman, S.D. Gunapala, M.T. Asom, J.M. Kuo and W.S. Hobson, "Photoexcited escape probability, optical gain, and noise in quantum well infrared photodetectors", *Jour. Appl. Phys.*, **72**, pp. 4429-4443, 1991.

Liu, W.W. and M. Fukuma, "Exact Solution of the Schrodinger Equation across an Arbitrary One-dimensional Piecewise-linear Potential Barrier", *Jour. Appl. Phys.*, **60**, pp. 1555-1559, 1986.

Liu, H.C., J. Li, J.R. Thompson, Z.R. Wasilewski, M. Buchanan and J.G. Simmons, "Multicolor voltage-tunable quantum-well infrared photodetector", *IEEE Electron. Dev. Lett.*, **14**, pp. 566-568, 1993.

Martinet, E., E. Rosencher, F. Luc, Ph. Bois, E. Costard and S. Delaitre, "Switchable bicolor (5.5-9.0 μm infrared detector using asymmetric GaAs/AlGaAs multiquantum well", *Appl. Phys. Lett.*, **61**, pp. 246-248, 1992.

Peng, L.H. and G.C. Fonstad, "Multiband Coupling Effects in Electron Quantum Well Intersubband Transitions", *Jour. Appl. Phys.*, **77**, pp. 747-754, 1995.

Shik, A. *Theory of Optical Intersubband Transitions in Quantum Wells*, ed. By E. Rosencher *et al.*, pp. 319-328, New York: Plenum Press, 1992.

Singh, J. *Physics of Semiconductors and their Heterostructures*, pp. 184-185, McGraw-Hill Book Co., 1993.

Ting, Mei, G. Karunasiri and S.J. Chua, "Two-color infrared detection using intersubband transitions in multiple step quantum wells with superlattice barriers", *Appl. Phys. Lett.*, **71**, pp. 2017-2019, 1997.

Tu, King-Ning, James W. Mayer and Leonard C. Feldman, *Electronic Thin Film Science for Electrical Engineers and Materials Scientists*, pp. 158, New York: Macmillan Publishing Co., 1992.

Vassel, M.O., J. Lee and H.F. Lockwood, "Multibarrier Tunneling in $Ga_{1-x}Al_xAs/GaAs$ Heterostructures", *Jour. Appl. Phys.*, **54**, pp. 5206-5213, 1983.

Vatannia, S. and G. Gildenblat, "Airy's Functions Implementation of the Transfer-Matrix Method for Resonant Tunneling in Variably Spaced Finite Superlattices", *IEEE Jour. Quan. Electron.*, **32**, pp. 1093-1105, 1996.

Vurguftman, I., J.R. Meyer and L.R. Ram-Mohan, "Band parameters for III-V compound semiconductors and their alloys", *Jour. Appl. Phys.*, **89**, pp. 5815-5875, 2001.

Wang, K.L. and P.G. Yuh, "Theory and Applications of Band-Aligned Superlattices", *IEEE Jour. Quan. Electron.*, **25**, pp. 12-19, 1989.

West, L.C. and S.J. Eglash, "First observation of an extremely large-dipole infrared transition within the conduction band of a GaAs quantum well", *Appl. Phys. Lett.*, **46**, pp. 1156-1158, 1985.

Yariv, Amnon *Optical Electronics in Modern Communications*, pp. 162, Oxford University Press, 1997

Yu, L.S. and S.S. Li, "A metal grating coupled bound-to-miniband and transition GaAs multiquantum well/superlattice infrared detector", *Appl. Phys. Lett.*, **59**, pp. 1332-1334, 1991.

Yuh, P.F. and K.L. Wang, "Optical transitions in a step quantum well", *Jour. Appl. Phys.*, **65**, pp. 4377-4381, 1989.

THIS PAGE INTENTIONALLY LEFT BLANK

INITIAL DISTRIBUTION LIST

1. Defense Technical Information Center
   Ft. Belvoir, Virginia

2. Dudley Knox Library
   Naval Postgraduate School
   Monterey, California

3. Chairman (Code PH)
   Department of Physics
   Naval Postgraduate School
   Monterey, California

4. Professor Gamani Karunasiri
   Department of Physics
   Naval Postgraduate School
   Monterey, California

5. Professor James Luscombe
   Department of Physics
   Naval Postgraduate School
   Monterey, California

6. Ensign Kevin R. Lantz
   United States Navy
   250 Forest Ridge Rd. Apt. 45
   Monterey, CA 93940